LAWRENCE
LIVERMORE
NATIONAL
LABORATORY

LLNL-JRNL-401869

Intercomparison of model simulations of mixed-phase clouds observed during the ARM Mixed-Phase Arctic Cloud Experiment. Part I: Single layer cloud

S. A. Klein, R. B. McCoy, H. Morrison, A. Ackerman, A. Avramov, G. deBoer, M. Chen, J. Cole, A. DelGenio, J.-C. Golaz, T. Hashino, J. Harrington, C. Hoose, M. Khairoutdinov, V. Larson, X. Liu, Y. Luo, G. McFarquhar, S. Menon, R. Neggers, S. Park, M. Poellot, K. von Salzen, J. Schmidt, I. Sednev, B. Shipway, M. Shupe, D. Spangenberg, Y. Sud, D. Turner, D. Veron, M. Falk, M. Foster, A. Fridlind, G. Walker, Z. Wang, A. Wolf, S. Xie, K.-M. Xu, F. Yang, G. Zhang

March 3, 2008

Quarterly Journal of the Royal Meteorological Society

Disclaimer

Intercomparison of model simulations of mixed-phase clouds observed during the ARM Mixed-Phase Arctic Cloud Experiment. Part I: Single layer cloud

Stephen Klein[1], Renata McCoy[1], Hugh Morrison[2], Andy Ackerman[3], Alexander Avramov[4], Gijs deBoer[5], Mingxuan Chen[6], Jason Cole[7], Anthony DelGenio[3], Michael Falk[8], Michael Foster[9], Ann Fridlind[3], Jean-Christophe Golaz[10], Tempei Hashino[5], Jerry Harrington[4], Corinna Hoose[11], Marat Khairoutdinov[12], Vincent Larson[8], Xiaohong Liu[13], Yali Luo[14], Greg McFarquhar[15], Surabi Menon[16], Roel Neggers[17], Sungsu Park[18], Michael Poellot[19], Knut von Salzen[20], Jerome Schmidt[21], Igor Sednev[16], Ben Shipway[22], Matthew Shupe[23], Doug Spangenberg[24], Yogesh Sud[25], David Turner[5], Dana Veron[26], Gregory Walker[27], Zhien Wang[27], Audrey Wolf[3], Shaocheng Xie[1], Kuan-Man Xu[24], Fanglin Yang[28], and Gong Zhang[15]

[1]Lawrence Livermore National Laboratory, Livermore, CA, USA
[2]National Center for Atmospheric Research, Boulder, CO, USA
[3]NASA Goddard Institute for Space Studies, New York, NY, USA
[4]The Pennsylvania State University, University Park, PA, USA
[5]University of Wisconsin – Madison, Madison, WI, USA
[6]Colorado State University, Fort Collins, CO, USA
[7]University of British Columbia, Vancouver, BC, Canada
[8]University of Wisconsin – Milwaukee, Milwaukee, WI, USA
[9]Rutgers University, New Brunswick, NJ, USA
[10]NOAA Geophysical Fluid Dynamics Laboratory, Princeton, NJ, USA
[11]ETH Zurich, Institute for Atmospheric and Climate Science, Zurich, Switzerland
[12]State University of New York at Stony Brook, Stony Brook, NY, USA
[13]Pacific Northwest National Laboratory, Richland, WA, USA
[14]State Key Laboratory of Severe Weather, Chinese Academy of Meteorological Sciences, Beijing, China
[15]University of Illinois, Urbana, IL, USA
[16]Lawrence Berkeley National Laboratory, Berkeley, CA, USA
[17]KNMI, Utrecht, Netherlands
[18]University of Washington, Seattle, WA, USA
[19]University of North Dakota, Grand Forks, North Dakota, USA

[20]Canadian Center for Climate, Vancouver, British Columbia, Canada
[21]Navy Research Laboratory, Monterey, CA, USA
[22]Met Office, Exeter, United Kingdom
[23]Cooperative Institute for Research in Environmental Sciences, University of Colorado / NOAA, Boulder, CO, USA
[24]NASA Langley Research Center, Hampton, VA, USA
[25]NASA Goddard Space Flight Center, Greenbelt, MD, USA
[26]University of Delaware, Newark, DE, USA
[27]University of Wyoming, Laramie, WY, USA
[28]National Centers for Environmental Prediction, Camp Springs, MD, USA

To be submitted to *Quarterly Journal of the Royal Meteorological Society* xxx 2008;
Revised, xxx 200x; Accepted, xxx 200x

Abstract

Results are presented from an intercomparison of single-column and cloud-resolving model simulations of a cold-air outbreak mixed-phase stratocumulus cloud observed during the Atmospheric Radiation Measurement (ARM) program's Mixed-Phase Arctic Cloud Experiment. The observed cloud occurred in a well-mixed boundary layer with a cloud top temperature of –15°C. The observed liquid water path of around 160 g m^{-2} was about two-thirds of the adiabatic value and much greater than the mass of ice crystal precipitation which when integrated from the surface to cloud top was around 15 g m^{-2}.

The simulations were performed by seventeen single-column models (SCMs) and nine cloud-resolving models (CRMs). While the simulated ice water path is generally consistent with the observed values, the median SCM and CRM liquid water path is a factor of three smaller than observed. Results from a sensitivity study in which models removed ice microphysics indicate that in many models the interaction between liquid and ice-phase microphysics is responsible for the large model underestimate of liquid water path.

Despite this general underestimate, the simulated liquid and ice water paths of several models are consistent with the observed values. Furthermore, there is some evidence that models with more sophisticated microphysics simulate liquid and ice water paths that are in better agreement with the observed values, although considerable scatter is also present. Although no single factor guarantees a good simulation, these results emphasize

1 the need for improvement in the model representation of mixed-phase microphysics.

2 This case study, which has been well observed from both aircraft and ground-based
3 remote sensors, could be a benchmark for model simulations of mixed-phase clouds.

1. Introduction

The treatment of clouds continues to be a highly challenging aspect of climate and weather modeling. The parameterization of Arctic clouds has been especially difficult, given the paucity of observations in the region (Curry et al. 1996). However, several field programs in recent years have begun to address this deficiency, including the 1994 Beaufort and Arctic Storms Experiment (Curry et al. 1997), 1997-1998 Surface Heat Budget of the Arctic Ocean Experiment (SHEBA, Uttal et al. 2002), the 1998 First International Satellite Cloud Climatology Project Regional Experiment – Arctic Clouds Experiment (Curry et al. 2000), and the ongoing ARM program site operating near Barrow, Alaska (Ackerman and Stokes 2003).

A major finding from these experiments was the observed frequency and persistence of supercooled liquid water and mixed-phase stratiform clouds throughout the year (Curry et al. 2000, Pinto et al. 2001, Intrieri et al. 2002, Shupe and Intrieri 2004). In contrast to mid-latitude cloud systems, there is little temperature dependence for the amount of liquid versus ice in Arctic mixed-phase clouds (Curry et al. 2000, McFarquhar and Cober 2004, Turner 2005). These clouds may contain one or more thin liquid layers embedded within a deep cloud that extends from near the surface into the middle and upper troposphere (Pinto 1998, Hobbs and Rangno 1998, Shupe et al. 2006). Ice crystals fall from the liquid layers and may reach the ground in the form of light snow or snow showers. During SHEBA, slightly more than half of the mixed-phase clouds consisted of a single low-level liquid layer, while the rest contained multiple liquid layers in a deep

cloud ice layer (Shupe et al. 2006).

The frequent occurrence of mixed-phase clouds has important implications for the cloud radiative forcing at the surface and the surface energy budget, since mixed-phase clouds tend to be optically thicker than ice-only clouds (Sun and Shine 1994, Shupe and Intrieri 2004, Turner 2005, Zuidema et al. 2005). The presence of mixed-phase rather than ice-only clouds may also significantly impact the structure of the boundary layer and large-scale dynamics through the influence of cloud-top radiative cooling (Morrison and Pinto 2006).

Climate and weather models tend to have difficulty predicting the observed frequency and persistence of Arctic mixed-phase clouds, leading to biases in surface radiative fluxes (Curry et al. 2000, Girard and Curry 2001, Morrison et al. 2003, Morrison and Pinto 2006, Morrison et al. 2005b, Inoue et al. 2006, Prenni et al. 2007). Studies have suggested that a more robust treatment of the modelled cloud microphysics is needed to improve simulations. Models with less sophisticated microphysics may incorrectly prescribe a ratio of liquid to ice mass that is inconsistent with Arctic observations. However, models with separate prognostic variables for liquid and ice and detailed microphysics may also produce poor simulations (Morrison et al. 2003, Inoue et al. 2006, Prenni et al. 2007). In these models, a more realistic treatment of ice microphysics, and in particular the number concentration of both small ice and snow, may be needed to improve results. Numerous modeling studies have demonstrated a strong sensitivity of mixed-phase clouds to ice number concentration (Pinto 1998, Harrington et al. 1999,

Jiang et al. 2000, Morrison and Pinto 2006, Prenni et al. 2007). Prenni et al. (2007) substantially improved their simulation of mixed-phase clouds by reducing ice nuclei number concentrations, which influence ice crystal number concentrations, from values typical of mid-latitudes to the low values observed in the Arctic. Their simulation was also sensitive to the representation of scavenging of ice nuclei by ice precipitation. Morrison and Pinto (2006) improved their simulation of Arctic mixed-phase stratus by reducing the specified intercept parameter of the snow size distribution; this is equivalent to reducing the snow number concentration for a given snow mixing ratio. These results increase the importance of resolving the long-standing uncertainty in the primary ice formation mechanisms in these clouds (Fridlind et al. 2007).

To further our understanding of Arctic mixed-phase cloud processes and provide a detailed observational dataset for model evaluation, ARM conducted the Mixed-Phase Arctic Cloud Experiment (M-PACE, Verlinde et al. 2007) over northern Alaska and the adjacent Arctic Ocean during September and October 2004. During M-PACE, a suite of in-situ and remote sensors gathered measurements of mixed-phase cloud microphysics, dynamics, radiation, and aerosol. Already, several studies have used M-PACE observations to assess single-column, cloud-resolving, mesoscale, weather and climate model simulations of mixed-phase clouds (Xie et al. 2006, Fridlind et al. 2007, Liu et al. 2007b, Luo et al. 2008a, Luo et al. 2008b, Prenni et al. 2007, Morrison et al. 2008a, Xie et al. 2008).

The present study compares simulations of mixed-phase clouds observed during M-

PACE using SCMs and CRMs. The current paper, Part I examines results for a single-layer mixed-phase stratocumulus cloud. The accompanying paper, Part II (Morrison et al. 2008b) examines results for a deeper, multi-layered mixed-phase cloud. The goals are to document the current state of simulations for two common types of Arctic mixed-phase clouds, to understand the sources of differences in the simulations, and to spur improvements in the representation of mixed-phase clouds in climate and weather models. Herein, the approach is taken to subject each model to the same initial condition and advective tendencies of the large-scale circulation as was done in previous model intercomparison studies performed under the auspices of the Global Energy and Water Experiment Cloud Systems Study (GCSS) project (Randall et al. 2003). This intercomparison is the first such activity of the GCSS Polar Cloud Working Group and was performed jointly with the ARM Cloud Modeling Working Group.

The next section describes the synoptic situation for the single-layer mixed-phase stratocumulus that is the subject of this paper. Section 3 describes the cloud property observations from the in-situ and ground-based remote sensors that are used to assess model simulations. Section 4 details the case specifications while Section 5 describes the seventeen SCMs and nine CRMs that participated in the intercomparison. Section 6 compares model simulations to the available observations and Section 7 describes the result of two sensitivity studies that were performed to obtain some insight into model differences. Section 8 briefly summarizes the key findings.

2. Synoptic situation

The boundary layer cloud system that is the focus of this study occurred during a period of northeasterly flow around an anticyclone to the north of Alaska (Verlinde et al. 2007). As the cold air above the sea ice to the northeast of Alaska flowed over the ice-free ocean adjacent to the coast, significant surface heat fluxes of temperature and water vapor induced the formation of boundary layer clouds in the form of "rolls" or "cloud-streets" which are common in "cold-air outbreak" stratocumulus (Figure 1). With the surface forcing, the boundary layer, as observed at the Alaska coast, was "well-mixed". This was demonstrated by the fact that the vertical profiles of water vapor and potential temperature match those in which the variables of water and energy that are conserved during the condensation process are uniform in the boundary layer (Figure 2).

During the period of focus for this study, 17Z 9 October to 5Z 10 October 2004, the boundary layer was between 1000 and 1500 m deep at the coast of Alaska. As observed by both aircraft and ground-based remote sensors, the upper half of the boundary layer contained a mixed-phase cloud with a cloud top temperature of about –15°C. This cloud contained an amount of liquid water which in terms of condensate mass far exceeded the amount of ice present in the cloud. Beneath the cloud base, which is identified here as the lowest level to contain liquid water, ice crystal precipitation occurred that reached the surface. The boundary layer was capped by a weak inversion of about 2K with dry and cloudless skies above.

3. Cloud observations

a. Aircraft observations

During this period, there were two flights of the University of North Dakota Citation (McFarquhar et al. 2007b). The Citation performed a number of spirals above Barrow and Oliktok Point as well as ramped ascents or descents along the coastline between the two stations. From the two flights, there are a total of thirty-two vertical profiles which are analyzed in this study.

On board were probes that measured the size distribution of particles with diameters between 3 μm and 40 mm, as well as the total condensate and liquid water contents separately. Cloud phase was determined to be either liquid only, ice only, or mixed-phase from an algorithm that considered the output of an icing detector, visual inspection of particle images, and the shape of the particle size distribution. The phase classification was made for each 30 sec flight segment that was determined to contain cloud. A 30 sec segment corresponds approximately to 2500 m of horizontal distance.

In addition to cloud phase, bulk parameters including the water contents, effective radii, and particle number concentrations were determined separately for liquid and ice. For ice-phase clouds, the bulk parameters are deduced only from particles with maximum dimensions greater than 53 μm because the shattering of large crystals on the protruding tips of probes used to measure small crystals may artificially enhance concentrations of small particles (McFarquhar et al. 2007a). The liquid effective radius is calculated as

the ratio of the third moment to the second moment of the liquid droplet size distribution. The effective radius of ice, r_i^{eff}, is calculated using the definition of Fu (1996) as $r_i^{eff} = \sqrt{3} IWC / 3\rho_i A_c$, where IWC is the ice water content, ρ_i is a bulk ice density assumed to be 910 kg m^{-3}, and A_c is the projected cross-sectional area of ice crystals. Rough estimates of uncertainty are $\pm 15\%$ for the bulk liquid parameters and a factor of two for the bulk ice parameters. For further details, see McFarquhar et al. (2007b).

b. Ground-based remote sensor observations

Cloud physical and dynamical properties and surface radiative fluxes have been retrieved from the active and passive sensors deployed at Barrow and Oliktok Point. Two sets of mixed-phase cloud retrievals are available (Turner 2005, Shupe et al. 2006, Shupe 2007, Turner et al. 2007, Shupe et al. 2008, hereafter termed SHUPE-TURNER; Wang and Sassen 2002, Wang 2007, hereafter termed WANG). The retrievals primarily rely on measurements from the millimeter wavelength cloud radar, lidar, and microwave radiometer. Except for liquid water path, cloud property retrievals are available only at Barrow.

Retrieved cloud physical properties include cloud top and base, cloud phase, the vertical profiles and vertically integrated amounts of liquid and ice water content, and the effective particle sizes of liquid and ice. Using a multi-sensor approach, Shupe (2007) derive a cloud phase mask that distinguishes target volumes into ice,

liquid, mixed-phase, or clear categories. Although vertical profiles of liquid water content can be derived by scaling an assumed adiabatic liquid water profile to the observed liquid water path, in this study models are compared only to the microwave radiometer liquid water path of which two estimates are available (Turner et al. 2007, hereafter termed TURNER; WANG). Cloud ice properties are derived from seasonally-tuned radar retrievals (Shupe et al. 2006) or from a combined radar-lidar method (Wang and Sassen 2002). For this case study, rough uncertainty estimates are $\pm 15\%$ for the bulk liquid parameters and a factor of two for the bulk ice parameters, similar to that of the aircraft data. In addition, cloud-scale vertical velocities are deduced from the cloud radar Doppler spectra under the assumption that the liquid cloud droplets trace the vertical air motions (Shupe et al. 2008). The time resolution of the remote sensing data is approximately 1 min which corresponds to a horizontal wind-advection distance of 800 m.

4. Case specifications

Because of the role of the ocean surface fluxes in cloud formation, it was assumed that models were above an ocean surface with forcing specified in the manner of previous GCSS boundary layer cloud working group intercomparisons (Stevens et al. 2005, Zhu et al. 2005). The initial condition for all models was a cloud-topped boundary layer that was well-mixed and capped by an inversion. In terms of the ice-liquid-water potential temperature θ_{li} and total water mixing ratio q_t which are conserved variables under

adiabatic conditions, these initial conditions were specified as:

$$\theta_{li} = \begin{cases} 269.2\text{K} & \text{for } p > p_{inv} \\ 275.33\text{K} + 0.0791\ \text{K hPa}^{-1} \times (815\,\text{hPa} - p) & \text{for } p < p_{inv} \end{cases} \quad (1)$$

$$q_t = \begin{cases} 1.95\ \text{g kg}^{-1} & \text{for } p > p_{inv} \\ 0.291\ \text{g kg}^{-1} + 0.00204\ \text{g kg}^{-1}\ \text{hPa}^{-1} \times (p - 590\,\text{hPa}) & \text{for } p < p_{inv} \end{cases} \quad (2)$$

where p is atmospheric pressure and p_{inv} is the inversion pressure with a value of 850 hPa. The total water mixing ratio q_t is defined as $q_t = q_v + q_l + q_i$, where q_v, q_l and q_i are the mixing ratios of water vapor, liquid water and ice water, respectively. The definition of θ_{li} used here is:

$$\theta_{li} = T \times (p_0 / p)^{R_d / c_p} \times \exp(-(L_v q_l + L_s q_i) / c_p T_{cb}) \quad (3)$$

where T is the absolute temperature, p_0 is a reference pressure of 1000 hPa, T_{cb} is the cloud base temperature of 263K, R_d is the dry air gas constant, c_p is the specific heat capacity of dry air at constant pressure, L_v and L_s are the latent heats of vaporization and sublimation, respectively. Figure 2 displays the initial conditions of the potential temperature and the mixing ratios of water vapor and liquid water which are consistent with (1) and (2).

Note that the initial phase of the cloud was specified to be pure liquid. It was assumed

that the microphysics present in the model would develop ice during the simulation and that a microphysical steady state would occur after a few hours of model spin-up. The lower boundary condition was specified as an ocean surface with temperature 274.01K. Models were asked to simulate the 12 hr starting from 17Z 9 October 2004.

For advective forcing of models in an Eulerian system, one must specify the horizontal advection of temperature and water vapor as well as the vertical velocity from which models can calculate the vertical advection of temperature and water vapor. These forcings were based upon analysis data from the European Centre for Medium-Range Weather Forecasts (ECMWF) for the ocean region 200 km upstream from the coastline between Barrow and Oliktok Point. The ECMWF data for these forcings were idealized to:

$$-\vec{V} \bullet \nabla T = \min\left[-4, -15 \times (1 - ((p_s - p)/218.18\,\text{hPa}))\right] \quad \text{K day}^{-1} \quad (4)$$

$$-\vec{V} \bullet \nabla q_v = \min\left[-0.164, -3 \times (1 - ((p_s - p)/151.71\,\text{hPa}))\right] \ \text{g kg}^{-1}\,\text{day}^{-1} \quad (5)$$

$$\omega = \min\left[D \times (p_s - p), D \times (p_s - p_{inv})\right] \quad (6)$$

where $-\vec{V} \bullet \nabla T$ is the temperature tendency from horizontal advection, $-\vec{V} \bullet \nabla q_v$ is the mixing ratio tendency from horizontal advection, and ω is the vertical pressure velocity (Figure 3). In these equations, p_s is the surface pressure and D is the large-scale divergence with values of 1010 hPa and 5.8×10^{-6} s^{-1}, respectively. The idealization of the ECMWF data was made in order to have vertically smooth forcing profiles that

minimize drifts in the temperature and water vapor above the boundary layer.

Lacking in-situ observations and in order to minimize model differences, the surface fluxes are specified from ECMWF data with values of 136.5 W m^{-2} for sensible heat and 107.7 W m^{-2} for latent heat. These surface fluxes imply a turbulent boundary layer as the convective velocity scale (Stull 1988, p. 355) is approximately 1 m s^{-1}. Furthermore, radiation calculations with the observed cloud (Section 6g) suggest that there is a significant longwave radiative cooling of 70 W m^{-2} at cloud top. With turbulence being forced from below and above, it is not surprising that the boundary layer is approximately well-mixed. One confirmation of the turbulent nature of the boundary layer is that the SHUPE-TURNER cloud radar retrievals of vertical velocities suggest a typical vertical velocity of 0.8 m s^{-1} inside the cloud.

Besides the buoyancy forcing from the top and bottom of the boundary layer, strong horizontal winds were present which imply a significant surface stress which also induces mixing. Models were asked to maintain the mean boundary layer wind close to the observed values of –13 m s^{-1} in the zonal direction and –3 m s^{-1} in meridional direction and most models used nudging to accomplish this. Radiation calculations in both the solar and longwave portion of the spectrum were performed by each model using their own predicted atmospheric state and radiation parameterization.

The following aerosol characteristics, more fully discussed in Morrison et al. (2008a), were recommended to the models that have an explicit aerosol-cloud coupling. For the

aerosol size distribution, a bimodal lognormal dry aerosol size distribution was fitted to the available observations. The size distribution for each mode is given by

$$\frac{dN}{d\ln r} = \frac{N_t}{\sqrt{2\pi}\ln\sigma}\exp\left[-\frac{\ln^2(r/r_m)}{2\ln^2\sigma}\right] \quad (7)$$

where N is the number concentration of aerosols and r is the particle radius. The parameters N_t, r_m, and σ are total number concentration, geometric mean radius, and standard deviation of each particle mode. For the smaller particle mode, these parameters have values of 72.2 cm^{-3}, 0.052 μm, and 2.04, respectively. For the larger particle mode, these parameters have values of 1.8 cm^{-3}, 1.3 μm, and 2.5, respectively. The aerosol composition was assumed to be ammonium bisulfate with an insoluble fraction of about 30% (Fridlind et al. 2000).

The amount of ice nuclei is an important parameter for models that simulate the number concentration of ice crystals. The Continuous Flow Diffusion Chamber on the Citation measured the ice nuclei with a diameter less than 2 μm acting in deposition, condensation-freezing, and immersion-freezing modes (Prenni et al. 2007). No measurement of ice nuclei acting in contact mode was possible. The measurements indicate extremely low amounts of ice nuclei with 85% of measurements having ice nuclei beneath background levels of 0.1 L^{-1} (Verlinde et al. 2007). Of the measurements with ice nuclei above background, the maximum concentration was about 10 L^{-1}. The

mean of all observations including those beneath background levels was 0.16 L^{-1}.

More information on the intercomparison specifications and plots of model simulations and observational data are available from http://science.arm.gov/wg/cpm/scm/scmic5/index.html.

5. Model descriptions

a. Overview

Tables 1 & 2 encapsulate the relevant characteristics of the seventeen SCMs and nine CRMs that took part in this intercomparison.

Among the SCMs, there are versions of two operational weather prediction models (ECMWF and NCEP) and five operational climate models (CCCMA, ECHAM, GFDL, GISS, and SCAM3). There are four SCMs which have primarily been used in research studies (ARCSCM, MCRAS, SCRIPPS, and UWM). Finally, there are six SCMs which include single modifications of the base set of SCMs (ECMWF-DUALM, GISS-LBL, MCRASI, SCAM3-LIU, SCAM3-MG, and SCAM3-UW). Four of these six include modifications to the representation of cloud microphysics: three SCMs add double moment microphysics (MCRASI, SCAM3-LIU, and SCAM3-MG) and one adds bin resolved cloud microphysics (GISS-LBL). Two of these six include modifications to the representation of boundary layer turbulence (ECMWF-DUALM and SCAM3-UW). The number of vertical levels in the boundary layer varies from four to fifty-one with a

median value of seven.

Among the CRMs, five are two-dimensional (NMS-BULK, NMS-SHIPS, RAMS-CSU, UCLA-LARC, UCLA-LARC-LIN), and four are three-dimensional (COAMPS®, DHARMA, METO, and SAM). There is a wide variety of horizontal and vertical resolutions as well as total domain represented. The two-dimensional models typically have horizontal and vertical resolutions of order 1000 m and 100 m, respectively, whereas the three-dimensional models typically have horizontal and vertical resolutions of 50 m in both directions. The number of vertical levels in the boundary layer varies from seven to seventeen for the two-dimensional models and from twenty-seven to sixty-four for the three-dimensional models. Total domain size is order 100 km for the two-dimensional models and 5000 m by 5000 m for the three-dimensional models. Thus, configurations of the two-dimensional models are typical of models commonly referred to as "cloud-resolving models" whereas the configurations of the three-dimensional models are typical of models commonly referred to as "large-eddy simulations".

b. Cloud microphysics

As the representation of cloud microphysics may be central to the ability of models to simulate a mixed-phase cloud, a brief summary of the microphysics used in these models is now given. Readers seeking more detail should consult the references in Tables 1 and 2.

The parameterizations of cloud microphysics can be classified into four

categories which span the range of detail used in today's cloud models. The simplest representation, which will be called "single moment with T-dependent partitioning", employs a single prognostic variable for the mass of cloud condensate and uses a temperature-dependent function to partition the relative amounts of liquid and ice. The relative amount of liquid at the cloud-top temperature of –15°C varies from 12% to 83% in the six SCMs (ECMWF, ECMWF-DUALM, MCRAS, NCEP, SCAM3, SCAM3-UW) and one CRM (SAM) that have this type of microphysical representation. Note that SAM also employs a temperature-dependent partitioning to determine the relative amounts of rain, snow, and graupel which at –15°C are 0%, 42%, and 58%, respectively.

The second class of cloud microphysics, "single moment with independent liquid and ice", employs separate prognostic variables for the mass of cloud liquid and ice in which the relative amounts of liquid and ice are not solely a function of temperature. Five SCMs (CCCMA, GFDL, GISS, SCRIPPS, and UWM) and one CRM (UCLA-LARC-LIN) employ this class of microphysics. In these models, the considerations which determine the relative amounts of liquid and ice typically include a temperature dependent partitioning of liquid and ice at cloud formation and subsequent conversion of liquid to ice through riming, droplet freezing, or the Bergeron effect which in mixed-phase clouds favors the growth of ice over liquid due to ice's lower saturation vapor pressure.

The third class of cloud microphysics, "double moment", employs prognostic variables for both the mass of condensate as well as the number concentration of cloud particles. Five SCMs (ARCSCM, ECHAM, MCRASI, SCAM3-LIU, SCAM3-MG) and five

CRMs (COAMPS®, METO, NMS-BULK, RAMS-CSU, UCLA-LARC) employ this approach. An advantage over the previous two classes is that a prognostic representation of number concentration potentially allows for a physically based coupling of clouds with aerosols. While not every condensate species may be represented with a prognostic variable for number concentration, all double moment parameterizations in this study represent the number concentration of cloud (or small) ice with a prognostic variable.

The fourth class of cloud microphysics, "bin microphysics", represents the number concentration of particles of different sizes with prognostic variables. This is the most complete representation of microphysics used in this study and is used in one SCM (GISS-LBL) and two CRMs (DHARMA and NMS-SHIPS). In DHARMA and NMS-SHIPS, twenty size bins each are used to represent liquid and ice particles. DHARMA has forty additional size bins for the mass of dissolved solute in each of the liquid drop or ice crystal size bins. GISS-LBL uses thirty-three size bins to represent liquid droplets and six classes of solid or partially solid condensate which include plates, columns, dendrites, snow, graupel, and frozen drops.

In general, only models with double moment or bin microphysics represent the dependence of cloud properties on aerosols. However, three models with double moment parameterizations of cloud microphysics do not have an explicit dependence of cloud properties on aerosols (COAMPS®, METO, NMS-BULK). Of the twelve models in which cloud properties depend on aerosols (ARCSCM, CCCMA, DHARMA, ECHAM, GISS-LBL, MCRAS, MCRASI, NMS-SHIPS, RAMS-CSU, SCAM3-LIU, SCAM3-MG,

UCLA-LARC), two models couple only the liquid-phase microphysics (CCCMA and MCRAS) while two others couple only the ice-phase microphysics (NMS-SHIPS and RAMS-CSU). Unfortunately, not all models alter their default aerosol representation to that recommended in the intercomparison specifications. In all models except DHARMA and RAMS-CSU, aerosols are fixed in time and thus a two-way coupling of aerosols and clouds is not present. In these models, ice nuclei are prognosed.

6. Results

a. Cloud and hydrometeor fraction

Figure 4 displays the height profile of the average cloud fraction from the observations and model simulations. For the observations, one of the profiles is deduced from the ground-based remote sensors at Barrow (SHUPE-TURNER) and the other two are from the two aircraft flights during the period. The aircraft cloud fraction depicts the fraction of time in a flight in which a given altitude was between cloud base and cloud top. For the remote sensors, cloud top is defined as the altitude of the highest range gate with significant radar return and cloud base is defined from the laser ceilometer which corresponds in this case to the lowest altitude with a significant amount of liquid water. For the aircraft, cloud top is defined as the highest altitude with significant cloud liquid or ice and cloud base is defined as the lowest altitude with a significant amount of liquid water (McFarquhar et al. 2007b).

Figure 4 indicates that the cloud bases and tops and cloud thicknesses are greater in

the retrievals from the ground-based remote sensors at Barrow than they are in those determined from the aircraft data. Some of these differences are due to a strong east-west gradient in cloud top, base and thickness which was observed by the aircraft which flew between Oliktok Point and Barrow. For example, the easternmost spirals near Oliktok Point in both flights have cloud tops of 950 to 1000 m whereas the westernmost spirals near Barrow have cloud tops of 1300 to 1500 m. The east-west gradient in geometrical cloud thickness is consistent with the greater liquid water path retrieved from the microwave radiometer at Barrow relative to that of Oliktok Point (Table 3). It is also consistent with the satellite image of Figure 1 which shows that the typical roll width, which is generally positively correlated to the depth of the boundary layer, is greater at Barrow than at Oliktok Point.

Similar to the observations, SCMs and CRMs produce a solid cloud layer between 700 and 1300 m (Figure 4). To construct each model cloud fraction panel, the cloud fraction for each model was averaged over the 12 hr simulation omitting the first 3 hr for model spin-up. From the set of cloud fraction profiles, the values of cloud fraction at each height which correspond to the median, minimum, maximum and 25^{th} and 75^{th} percentiles of models were calculated at each altitude. The model panels show the median cloud fraction (solid black line), the inner 50% of models (the darker shaded area), and the range of the data (the area of both the lighter and darker shading). All CRMs were asked to compute cloud fraction which was defined as the fraction of grid volumes with cloud droplet mixing ratios greater than 0.01 g kg^{-1} or ice mixing ratios greater than 0.0001 g kg^{-1}. These thresholds were chosen to approximately match the sensitivities of the

aircraft data. For SCMs, cloud fraction is an inherent property of the model which is generally thought to mean the horizontal fraction of a grid-cell that is saturated and contains either cloud liquid or ice.

Both the observed and modeled clouds produced precipitation. This is shown in a plot of the hydrometeor fraction (Figure 5), which is defined as the area fraction which contains either cloud or precipitation. From the observations, this was calculated using the presence of any liquid or ice condensate from the remote sensor retrievals. For the models, this was calculated using either the presence of cloud, as defined above, or rain, snow, or graupel mixing ratios in excess of 0.0001 g kg^{-1}. The remote sensors indicate that the cloud continually produced precipitation which reached the surface.

As to the phase of the hydrometeors, the phase classifications from the aircraft data and the remote sensors (SHUPE-TURNER) are consistent (Figure 6). This figure displays the fraction of time that a given phase occurred composited on a normalized height coordinate where –1 is the surface, 0 is cloud base, and +1 is cloud top. The observations indicate most of the cloud is mixed-phase (liquid and ice co-existing in the same volume) with ice-phase precipitation beneath the cloud. Liquid-phase only condensate is detected on occasion near the cloud top.

b. Liquid and ice water path

Although models generally produce an overcast precipitating cloud, substantial differences exist in the simulated phase partitioning and mass of cloud condensate.

Figure 7 shows a scatterplot of the median liquid water and ice water paths from the observations and the models. The observations are indicated by the letters on the plot: 'A' for aircraft data, 'S' for SHUPE-TURNER retrievals, and 'W' for WANG retrievals. The models are displayed with symbols that categorize a given model according to whether it is a SCM or CRM which is indicated by the symbol filling and the class of its microphysical scheme which is indicated by the symbol shape. Individual observational and model data are presented in Tables 3 and 4.

Because the observations do not distinguish cloud from precipitation condensate, the vertical integrals of the model condensate include precipitation condensate in the reported liquid and ice water paths. For the liquid-phase, the contribution of rain to the total water path is always much smaller than the contribution of cloud droplets, whereas for the ice-phase, the contribution of snow is often equal to or larger than the contribution of the small ice. Graupel makes little or no contribution to the total ice water path in the CRMs. Note that for the SCMs, the contribution of rain and snow must be calculated from the vertical profiles of the precipitation rate as the mixing ratios of rain and snow are generally not prognostic variables in SCMs. These precipitation rates were unavailable from some SCMs (ECHAM, GISS, McRAS, McRASI, NCEP, and SCRIPPS).

The observations indicate that the cloud system was water dominated. The retrievals from the ground-based remote sensors at Barrow indicate a liquid water path of about 200 g m^{-2}, whereas the aircraft liquid water path, which is determined from a vertical integral of the profile data, is lower with values around 120 g m^{-2}. As mentioned previously, some

of this difference reflects the east-west gradient in cloud properties; this is further confirmed by the liquid water paths retrieved from the microwave radiometers at Oliktok Point which have values around 100 g m^{-2} (Table 3) which is about one-half of the value at Barrow. For the ice-phase, both the SHUPE-TURNER and WANG retrievals at Barrow suggest 30 g m^{-2} of ice whereas the aircraft observations suggest far lower values of around 5 g m^{-2}. In addition to the east-west gradient in cloud properties, some of this difference arises because the aircraft totals do not include ice from the lower 60% of sub-cloud air which the aircraft did not sample (Figure 6). Taking into account these factors as well as the uncertainty in the measurements (Section 3), a best estimate of the liquid and ice water paths for this period and region would be 160 ± 50 g m^{-2} and 15 g m^{-2} ± a factor of two (i.e., the ice water path could be between 8 and 30 g m^{-2}), respectively.

The model simulations produce a wide range of results. Although more than three-quarters of the models have liquid water paths in excess of ice water paths as observed, two-thirds of the models underestimate the observed liquid water path. The median liquid and ice water paths differ little according to model type with values of 56.0 g m^{-2} and 57.3 g m^{-2} for the liquid-phase from SCMs and CRMs, respectively, and values of 29.1 g m^{-2} and 17.1 g m^{-2} for the ice-phase from SCMs and CRMs (Table 4). Thus, on average, the primary model deficiency is an underestimate of the amount of liquid present in the clouds. Despite this general underestimate, five models (DHARMA, SCAM3, SCAM3-LIU, SCAM3-UW, and UCLA-LARC) have liquid and ice water paths which are consistent with the best estimate of the observations, which is indicated by the lightly

dashed rectangle in Figure 7.

The median liquid and ice water paths appear to approach the observed values as the sophistication of the cloud microphysical parameterization increases. Specifically, the median liquid water path for the seven models with single moment with T-dependent partitioning is 21.2 g m^{-2}, whereas that for the six models with single moment with independent liquid and ice microphysics is 72.8 g m^{-2}, and that of the ten models with double moment microphysics is 100 g m^{-2}. The corresponding quantities for ice water path are 33.8, 31.8, and 19.9 g m^{-2}, among these models. However, the models with bin microphysics do not show improvement over the models with double moment microphysics, but there are only three models with this microphysical class.

Despite this general trend, use of a particular class of cloud microphysics does not guarantee a good simulation. For example, half of the ten models with double moment microphysics have liquid water paths less than 60 g m^{-2}, whereas the other the other half of these models have liquid water paths in excess of 140 g m^{-2}. The median liquid water path of 100 g m^{-2} is thus a statistical average of a bimodal population of models. Undoubtedly, differences in the representation of boundary layer turbulence or whether it is a SCM or CRM are also responsible for the spread of model results. This is illustrated by examination of two of the three pairs of models which use identical microphysics but differ in the formulation of boundary layer turbulence or whether it is a SCM or CRM. For both of these pairs (ECMWF and ECMWF-DUALM, and ARCSCM and UCLA-LARC, respectively), the total condensate water path differs by more than 100 g m^{-2}

demonstrating that the simulated cloud properties depend on more than the cloud microphysical scheme employed.

Aerosol-cloud coupling appears to improve the CRM simulations of liquid water path as all CRMs with coupling have liquid water paths greater than CRMs without aerosol-cloud coupling. However, two (NMS-SHIPS and RAMS-CSU) of the four CRMs with aerosol-cloud coupling produce virtually no ice which in the case of RAMS-CSU is due to precipitation scavenging of all of the initial ice nuclei. Furthermore, SCMs do not display stratification of liquid water paths by aerosol-cloud coupling. From this set of simulations, there does not appear to be a single feature of a model that guarantees a good simulation of the column integrated amount of liquid and ice; rather, it is likely that a good cloud simulation depends on several high-quality model components functioning well together.

c. Liquid and ice water content

The vertical distributions of liquid and ice water content from the observations and models on a normalized height coordinate are displayed in Figures 8 and 9. The aircraft measured liquid water content indicates that the liquid water content increases with height above cloud base which is a characteristic of adiabatic clouds in well-mixed boundary layers. However, the maximum aircraft liquid water content is smaller than the adiabatic value of the cloud top liquid water content which is 0.6 g m^{-3} for a cloud with the aircraft observed thickness of 600 m. The sub-adiabatic nature of the cloud is

consistent with depletion of liquid water by ice precipitation, although cloud-top entrainment may also contribute to the depletion. Because the vertical profile of liquid water content in mixed-phase clouds cannot currently be retrieved, no remote sensing panel for liquid water content is displayed in Figure 8. Despite this, the remote sensor retrievals also indicate that the cloud at Barrow is less than adiabatic as the retrieved liquid water path of 195 to 225 g m^{-2} is smaller than the adiabatic liquid water path which is between 235 and 270 g m^{-2} for the observed cloud thicknesses of 700 to 750 m at Barrow. Both SCMs and CRMs simulate greater liquid water content in the upper half of the cloud although this tendency is more apparent for the highest 25% of models than it is for the model median value. The low vertical resolution of some SCMs hinders a robust assessment of this point, however. Consistent with the liquid water path, the median model liquid water content is significantly smaller than observed.

The vertical profile of ice water content is generally more uniform than that of the liquid water content in both the aircraft and retrievals. The aircraft data indicate median values of 0.01 g m^{-3} which are fairly constant in the cloud and the portion beneath the cloud that the aircraft sampled. The WANG retrievals at Barrow indicate somewhat larger median values in the cloud than in the layer beneath, 0.02 to 0.03 g m^{-3} as compared to 0.01 to 0.02 g m^{-3}. SHUPE-TURNER retrievals are similar. Some of these differences between the aircraft and ground-based retrievals are probably due to the east-west gradient in cloud properties, although the differences are within the measurement uncertainty (Section 3). A feature of both the aircraft and ground-based retrievals is that the distribution of ice water content has a long positive tail with some values in excess of 0.1 g m^{-3}. The

model median values are in reasonable agreement with the observations for both the SCMs and CRMs. The models ice water content values are also somewhat greater in the cloud than in the layer beneath. A decrease in ice water content as one approaches the surface would be consistent with sublimation of ice in the sub-saturated layers near the surface.

d. Surface precipitation

The ice reaching the surface will be observed as surface precipitation. Unfortunately quantitative estimates of the surface snow rate are highly uncertain. The National Weather Service station in Barrow recorded 0.25 mm d^{-1} for this period. However, for an ice water mixing ratio of 0.01 g m^{-3} at the surface (Figure 9) with an assumed mass-weighted fall speed of 1 m s^{-1}, the precipitation rate would be 0.9 mm d^{-1}. The median surface snow rates of SCMs and CRMs are 0.70 and 0.41 mm d^{-1}, respectively. Although in most models the surface rain rate is zero or very much smaller than the snow rate, there are a few models (CCCMA, ECHAM, RAMS-CSU) in which all of the surface precipitation is in the form of rain. These models have a high liquid water path but are unable to produce enough ice so that ice precipitation would reach the surface.

e. Cloud microphysics

Figure 10 displays the mass-weighted effective radii and number concentrations of liquid and ice from the aircraft observations and the model simulations for which these diagnostics were available. The CRM liquid droplet effective radii exceed that of

the observations whereas the CRM cloud droplet number concentration is consistent with the aircraft data. The spread in SCM liquid droplet microphysical quantities is large, with the median effective radius consistent with the observations but the median cloud droplet number concentration in excess of the observations. Although these results appear inconsistent with the general underestimate of cloud liquid water content by both SCMs and CRMs, they may not be because the models that report effective radii and cloud droplet number have above average liquid water content.

For ice cloud properties, the range in ice effective radii from the SCMs and ice crystal number concentration from both the SCMs and CRMs is very large; among the CRMs, the ice crystal number concentration varies over 6 orders of magnitude. The spread of ice effective radius among the aircraft profiles shown in Figure 10 is artificially small due to the unavailability of the High-Volume Precipitation Sampler on the flights for this day. The median value of the ice crystal number concentration is smaller than observed for CRMs but consistent with the observations for the SCMs while the median value of ice effective radius is greater than observed for both the SCMs and CRMs. Note that the observed median ice crystal concentration of 2 L^{-1} is an order of magnitude larger than the measurements of ice nuclei. Possible reasons for this difference are extensively discussed in Fridlind et al. (2007). It is also noted that the comparison of ice cloud microphysics between models and observations is hindered by the fact that models may not have computed the ice effective radius with the same definition as used in McFarquhar et al. (2007b) or may not have limited the count of their ice crystal number

to particles with diameters greater than 53 μm as was done with the observations.

f. Thermodynamic structure

Figure 11 compares the time-averaged profiles of total water mixing ratio q_t and ice-liquid water potential temperature θ_{li} from the model simulations to the initial condition. The model underestimate of liquid water content is accompanied by a vertical gradient of q_t which differs from the initial conditions and is likely unrealistic. Note that a cloud with a liquid water content of two-thirds of the adiabatic value but a water vapor mixing ratio which follows the adiabatic profile of the initial condition (Figure 2) would have a value of q_t at cloud top that is only 0.15 g kg^{-1} lower than the value in the sub-cloud layer.

Ice precipitation would in absence of other effects try to stabilize the boundary layer by providing a net heating to the cloud layer and a net cooling to the sub-cloud layer. Although there is some evidence for stabilization in the CRM profiles of θ_{li}, the surface fluxes and cloud-top radiative cooling in models with a significant amount of liquid act to keep the boundary layer well-mixed and probably minimize the influence of ice precipitation on vertical stability. However, models which have greater amounts of cloud liquid water content do show smaller vertical gradients in q_t and θ_{li}.

g. Radiation

Figure 12 compares models simulations of the solar transmission to the radiation measurements at Barrow (OBS) and the results of two calculations from a radiative transfer model (STREAMER, Key and Schweiger 1998) that uses the initial condition sounding of temperature and water vapor and along with cloud liquid and ice water paths of 200 and 13 g m^{-2}, respectively. The solar transmission is computed as the average value for the period 17Z 9 October to 5Z 10 October 2004 of the downward shortwave radiative flux at the surface divided by that at the top-of-atmosphere. The solar transmission is plotted together with the total condensate water path, although it is understood that there are a number of reasons for why the points will not scatter along a single line. As might be expected from the model underestimate of liquid water path, models generally overestimate the solar transmission.

The model overestimate is greater than it appears because model simulations used an ocean surface. Given that the observations were over snow-covered land at Barrow, the observed solar transmission is enhanced by multiple reflections between the surface and the cloud. The impact of the different surface albedo can be assessed by comparing STREAMER calculations that use an ocean surface with low albedo (S-O) to those that use a snow-covered land surface with high albedo (S-L). Given that STREAMER calculations with the land surface have good agreement with the observations, it suggests that models should simulate solar transmissions closer to 0.1 than to 0.2.

In the Arctic, the downward component of longwave radiation at the surface is strongly affected by clouds and is an important quantity that affects the surface temperature of

over land and sea-ice. Although this effect has been disabled in these model simulations, it is still important to assess whether the simulated cloud has the correct radiative impact. STREAMER calculations with the observed cloud, either over an ocean or land surface, are consistent with the observed value of 280 W m^{-2} (Figure 13). As the downward longwave radiation is 200 W m^{-2} in clear-sky STREAMER calculations, the longwave cloud radiative effect is about 80 W m^{-2}. Given that the longwave emissivity of clouds is near unity after the condensate water path exceeds about 50 g m^{-2} (Stephens 1978), it would be expected and is found that models with total condensate water paths greater than this value would produce longwave cloud radiative effects consistent with the observations (Figure 13).

7. Sensitivity studies

a. No ice microphysics

Given that numerous modeling studies (Pinto 1998; Harrington et al. 1999; Jiang et al. 2000; Morrison and Pinto 2006; Prenni et al. 2007) have demonstrated that the amount of supercooled water in mixed-phase clouds is very sensitive to the representation of ice microphysics in general, and to the ice crystal number concentration in particular, it is of interest to determine this sensitivity with the present set of models. A sensitivity study was performed in which models were asked to simulate a hypothetical case of a liquid-phase cloud. A sensitivity study focused on the ice crystal number concentration was not performed because the liquid-only phase experiment is simple to construct and permits all

models to perform a meaningful simulation.

The results demonstrate that there is a large sensitivity of the integrated amount of condensate to the inclusion of ice microphysics (Figure 14). However, this is only true in the models which have condensate water paths less than 150 g m^{-2} in the control simulation. In these models, the condensate water path in the no ice microphysics experiment is greater than that of the control simulation and is often between 200 and 300 g m^{-2}. At least in these models, this suggests that excessive conversion of liquid to ice which easily precipitates is responsible for the underestimate of liquid water path. This is partially confirmed by Figure 15 which shows a general tendency for models which have a high fraction of ice in the control experiment to show the greatest relative increase in the condensate water path.

The spread in liquid water path among the SCMs and CRMs is still large in the no ice microphysics experiment. SCM liquid water paths vary from 60 to 580 g m^{-2}, while CRM liquid water paths vary from 65 to 330 g m^{-2}. This indicates that differences in the representation of processes such as liquid-phase microphysics and boundary layer turbulence can still lead to significant differences in the simulated liquid water path.

For the models which are sensitive to the inclusion of ice-phase microphysics, the boundary layer tends to be more well-mixed in q_t and θ_{li} relative to the same model in the control experiment and in the sensitive CRMs the boundary layer is slightly deeper. These effects are likely due to greater turbulence near cloud top which is driven by strong

cloud top radiative cooling common to stratocumulus.

b. Vertical resolution

Low vertical resolution in atmospheric models in general, and climate models in particular, may lead to non-convergence of simulated cloud properties. Yuan et al. (2006) found a significant decrease in the liquid and ice water paths as vertical resolution was increased in CCCMA SCM simulations of mixed-phase clouds observed during SHEBA. Models were asked to submit a simulation with higher vertical resolution. As the vertical resolution in this sensitivity study was not specified, the number of levels in the boundary layer varied from 14 to 146 in the SCMs and from 23 to 53 in the CRMs (Tables 1 and 2). Reassuringly, the results indicate a fairly small sensitivity to vertical resolution which is generally much less than the sensitivity to the inclusion of ice microphysics (compare Figure 16 to Figure 14). One SCM (SCAM3-LIU) did exhibit a pronounced sensitivity of cloud phase to vertical resolution (Table 4). This was due to a bug in the ice nucleation parameterization which has subsequently been corrected.

8. Summary

An intercomparison of single-column and cloud-resolving model simulations of cold-air outbreak mixed-phase stratocumulus has been presented and evaluated with the available ground-based and aircraft observations collected during the ARM Mixed-Phase Arctic Cloud Experiment. While the majority of models reproduce the observed structure of a mixed-phase cloud that produces ice precipitation, the median liquid water path

of both SCMs and CRMs is only one-third of the observed value. On the other hand, several models have simulated liquid and ice water paths which are consistent with the observations. Although a general underestimate of liquid water path in Arctic mixed-phase clouds has been found in previous studies (Inoue et al. 2006, Morrison and Pinto 2006, Prenni et al. 2007), the present study confirms this result in the context of a highly constrained modeling environment in which identical large-scale advective tendencies and surface fluxes have been applied to the models.

There is a trend towards better agreement with the observations of the liquid and ice water paths as the sophistication of the model microphysics increases from single moment with T-dependent partitioning to single moment with independent liquid and ice to double moment. While similar conclusions have been reached in some modeling studies involving Arctic clouds (Girard and Curry 2001, Morrison and Pinto 2006), this study involved a wider set of models than these earlier studies. However, also present is a considerable scatter among the models with a given class of microphysics, so it unclear how much significance to give to this trend. More discussion of this issue will be presented in Part II of this study where a similar trend is also observed.

A sensitivity study in which models simulated only a liquid-phase cloud shows that the interaction of ice microphysics with liquid microphysics is responsible for the significant underestimate of liquid water path present in many models. This calls attention to the processes such as the way ice is formed (the nucleation problem) and the rate at which ice crystals lower the water vapor beneath that necessary to sustain liquid water in the clouds

(the Bergeron process). A second sensitivity study showed much less dependence of the simulated liquid and ice water paths on the vertical resolution of the model.

There may not be a simpler setting for the simulation of mixed-phase clouds. Complications of multi-layer cloud systems (Curry et al. 1996) or strong feedbacks between the cloud and the surface temperature and fluxes that happen when mixed-phase clouds are above sea-ice (Morrison and Pinto 2006) have been eliminated in the present case. Despite this simplicity, few model simulations are consistent with the observations reflecting the difficulty of simulating these clouds. The intercomparison of model simulations of multi-layer clouds observed during M-PACE is presented in Part II of this study.

The relative simplicity of the cloud and its boundary conditions as well as the availability of high quality observations may make this case study suitable as a benchmark for mixed-phase clouds. Thin single layer clouds with high amounts of supercooled liquid water that produce ice precipitation are not limited to the Arctic, but also occurs in cold-air outbreaks at lower latitudes (Kristovich et al. 2000) and middle-level cloud systems (Fleishauer et al. 2002, Hogan et al. 2003). It is hoped that this case will continue to be an attractive target for cloud modelers.

Acknowledgements. This work is supported by the Office of Science of the United States (U. S.) Department of Energy under grants DE-FG02-02ER63337 (McFarquhar), DE-FG02-03ER63539 (Morrison), DE-FG02-05ER63955 (Cole), DE-FG02-05ER64058

(Harrington), DE-FG02-05ER64069 (Wang), DE-AI02-06ER64173 (Ackerman and Fridlind), DE-FG02-06ER64167 (Turner), DE-FG02-06ER64187 (deBoer), and DE-FG02-07ER64378 (McFarquhar). A. Ackerman and A. Fridlind are supported by the U. S. National Aeronautics and Space Administration's (NASA) Radiation Sciences Program and the NASA Advanced Supercomputing Division. J. Cole is supported by the Canadian Foundation for Climate and Atmospheric Sciences. M. Falk and V. Larson are supported by National Science Foundation (NSF) grant ATM-0442605 and subaward G-7424-1 from the Department of Defense Center for Geosciences/Atmospheric Research at Colorado State University via Cooperative Agreement DAAD19-02-2-0005 with the Army Research Laboratory. C. Hoose is supported by the climate program of the Swiss National Centre of Competence in Research. Y. Luo is supported by the Chinese Academy of Meteorological Sciences and NASA's Cloud Modeling and Analysis Initiative. H. Morrison is supported by NASA grant NNG06GBB1G and by the NSF Science and Technology Center for Multi-Scale Modeling of Atmospheric Processes, managed by Colorado State University under cooperative agreement ATM-0425247. The contribution of S. Klein, R. McCoy, and S. Xie to this work is performed under the auspices of the U. S. Department of Energy by Lawrence Livermore National Laboratory under contract DE-AC52-07NA27344. The Pacific Northwest National Laboratory is operated for the Department of Energy by Battelle Memorial Institute under contract DE-AC06-76RLO-1830. The National Center for Atmospheric Research is sponsored by the National Science Foundation. Gratitude is expressed to Anton Beljaars for providing ECMWF analysis data.

References

Ackerman, T. P. and G. Stokes, 2003: The Atmospheric Radiation Measurement program, *Physics Today*, **56**, 38-45.

Ackerman, A. S., M. P. Kirkpatrick, D. E. Stevens, and O. B. Toon, 2004: The impact of humidity above stratiform clouds on indirect aerosol climate forcing. *Nature*, **432**, 1014-1017, doi:10.1038/nature03174.

Boville, B. A., P. J. Rasch, J. J. Hack, and J. R. McCaa, 2006: Representation of clouds and precipitation processes in the Community Atmosphere Model Version 3 (CAM3). *J. Clim*, **19**, 2184–2198.

Bretherton, C. S. and S. Park, 2007: A moist turbulence and entrainment parameterization in the Community Atmosphere Model. *xxx.*, submitted.

Chen, S. and Coauthors, 2003: COAMPS® version 3 model description: General theory and equations. Navy Research Laboratory Publication #NRL/PU/7500-03-448.

Collins W. D. and Coauthors, 2006: The formulation and atmospheric simulation of the Community Atmosphere Model version 3 (CAM3). *J. Clim.*, **19**, 2144–2161.

Cotton, W. R. and Coauthors, 2003: RAMS 2001: Current status and future directions. *Meteor. Atmos. Phys.*, **82**, 5-29.

Curry, J. A., W. B. Rossow, D. Randall, and J. L. Schramm, 1996: Overview of Arctic cloud and radiation characteristics. *J. Clim.*, **9**, 1731-1764.

Curry, J. A., J. O. Pinto, T. Benner, and M. Tschudi, 1997: Evolution of the cloudy boundary layer during the autumnal freezing of the Beaufort Sea, *J. Geophys. Res.*, **102**, 13851–13860.

Curry, J. A. and Coauthors, 2000: FIRE Arctic Clouds Experiment. *Bull. Amer. Met. Soc.*, **81**, 5–29.

Environmental Modeling Center (EMC), 2003: The GFS atmospheric model. National Center for Environmental Prediction Office Note 442, U. S. Department of Commerce, National Oceanic and Atmospheric Administration, 14 pp. Available online at http://www.emc.ncep.noaa.gov/officenotes/FullTOC.html.

European Centre for Medium Range Weather Forecasts (ECMWF), 2007: IFS documentation cycle 31r1. Part IV: Physical processes. 155 pp. Available online at http://www.ecmwf.int/research/ifsdocs/CY31r1/index.html.

Ferrier, B., 1994: A double-moment multiple-phase four-class bulk ice scheme. Part I: Description. *J. Atmos. Sci.*, **51**, 249-280.

Flatau, P. J., G. J. Tripoli, J. Verlinde, and W. R. Cotton, 1989: The CSU-RAMS cloud microphysics module: General theory and code documentation. Colorado State

Department of Atmospheric Science paper no. 451.

Fleishauer, R. P., V. E. Larson, and T. H. Vonder Haar, 2002: Observed microphysical structure of midlevel mixed-phase clouds. *J. Atmos. Sci.*, **59**, 1779-1804.

Fridlind, A. M. and Coauthors, 2000: Analysis of gas-aerosol partitioning in the Arctic: Composition of size-resolved equilibrium model results with field data, *J. Geophys. Res.*, **105**, 19891-19904.

Fridlind, A. M. and Coauthors, 2007: Ice properties of single-layer stratocumulus during the Mixed-Phase Arctic Cloud Experiment (M-PACE): Part II. Model results. *J. Geophys. Res.*, **112**, D24202, doi:10.1029/2007JD008646.

Fu, Q., 1996: An accurate parameterization of the solar radiative properties of cirrus clouds. *J. Clim.*, **9**, 2058-2082.

The GFDL Global Atmospheric Model Development Team (GFDL GAMDT), 2004: The new GFDL global atmosphere and land model AM2-LM2: Evaluation with prescribed SST simulations. *J. Clim.*, **17**, 4641-4673.

Girard, E. and J. A. Curry, 2001: Simulation of Arctic low-level clouds observed during the FIRE Arctic Clouds Experiment using a new bulk microphysics scheme, *J. Geophys. Res.*, **106**, 15,139–15,154.

Golaz, J.-C., V. E. Larson, and W. R. Cotton, 2002: A PDF-based model for

boundary layer clouds. Part I: Method and model description. *J. Atmos. Sci.*, **59**, 3540-3551.

Golaz, J.-C., S. Wang, J. D. Doyle, and J. M. Schmidt, 2005: COAMPS®-LES: Model evaluation and analysis of second and third moment vertical velocity budgets. *Bound.-Layer Meteor.*, **116**, 487-517.

Hansen, J. and Coauthors, 2002: Climate forcings in Goddard Institute for Space Studies SI2000 simulations. *J. Geophys. Res.*, **107**, 4347, doi:10.1029/2001JD001143.

Harrington, J. Y., T. Reisen, W. R. Cotton, and S. M. Kreidenweis, 1999: Cloud resolving simulations of Arctic stratus. Part II: Transition-season clouds. *Atmos. Res.*, **51**, 45–75.

Hashino, T. and G. J. Tripoli, 2007: The spectral ice habitat prediction system (SHIPS). Part I: Model description and simulation of vapor deposition process. *J. Atmos. Sci.*, **64**, 2210-2237.

Hobbs, P. V. and A. L. Rangno, 1998: Microstructures of low and middle-level clouds over the Beaufort sea. *Quart. J. Roy. Meteor. Soc.*, **124**, 2035-2071.

Hogan, R. J. and Coauthors, 2003: Characteristics of mixed-phase clouds. I: Lidar, radar and aircraft observations from CLARE'98. *Quart. J. Roy. Meteor. Soc.*, **129**, 2089-2116.

Iacobellis, S. F. and R. C. J. Somerville, 2006: Evaluating parameterizations of the

1 autoconversion process using a single-column model and Atmospheric Radiation
2 Measurement Program measurements. *J. Geophys. Res.*, **111**, D02203,
3 doi:10.1029/2005JD006296.

4 Inoue, J., J. Liu, J. O. Pinto, and J. A. Curry, 2006: Intercomparison of Arctic regional
5 climate models: Modeling clouds and radiation for SHEBA in May 1998. *J. Clim.*, **19**,
6 4167-4178.

7 Intrieri, J. M., M. D. Shupe, T. Uttal, and B. J. McCarty, 2002: An annual cycle of Arctic
8 cloud characteristics observed by radar and lidar at SHEBA, *J. Geophys. Res.*, **107**, 8030,
9 doi:10.1029/2000JC000423.

10 Jiang, H. and Coauthors, 2000: Cloud resolving simulations of mixed-phase Arctic stratus
11 observed during BASE: Sensitivity to concentration of ice crystals and large-scale heat
12 and moisture advection. *J. Atmos. Sci.*, **57**, 2105–2117.

13 Key, J. R., and A. J. Schweiger, 1998: Tools for atmospheric radiative transfer: Steamer
14 and FluxNet. *Computers and Geosciences*, **24**, 443-451.

15 Khain, A. P., and I. Sednev, 1996: Simulation of precipitation formation in the Eastern
16 Mediterranean coastal zone using a spectral microphysics cloud ensemble model. *Atmos.*
17 *Res.*, **43**, 77-110.

18 Khairoutdinov, M. F., and D.A. Randall, 2003: Cloud-resolving modeling of the ARM

summer 1997 IOP: Model formulation, results, uncertainties and sensitivities. *J. Atmos. Sci.*, **60**, 607-625.

Kristovich, D. A. R. and Coauthors, 2000: The Lake—Induced Convection Experiment and the snowband dynamics project. *Bull. Amer. Meteor. Soc.*, **81**, 519–542.

Larson, V. E. and Coauthors, 2006: What determines altocumulus dissipation time? *J. Geophys. Res.*, **111**, D19207, doi:10.1029/2005JD007002.

Lin, Y.-L., R. Farley, and H. Orville, 1983: Bulk parameterization of the snow field in a cloud model. *J. Clim. Appl. Met.*, **22**, 1065-1092.

Liu, X. and J. E. Penner, 2005: Ice nucleation parameterization for global models. *Meteorologische Zeitschrift*, **22**, 1065-1092.

Liu, X., J. E. Penner, S. J. Ghan, and M. Wang, 2007a: Inclusion of ice microphysics in the NCAR Community Atmospheric Model version 3 (CAM3). *J. Clim.*, **20**, 4526-4547.

Liu X., S. Xie, and S. J. Ghan, 2007b: Evaluation of a new mixed-phase cloud microphysics parameterization with CAM3 single-column model and M-PACE observations. *Geophys. Res. Lett.*, **34**, L23712, doi:10.1029/2007GL031446.

Lohmann, U., P. Stier, C. Hoose, S. Ferrachat, S. Kloster, E. Roeckner, and J. Zhang, 2007: Cloud microphysics and aerosol indirect effects in the global climate model

ECHAM5-HAM. *Atmos. Chem. Phys.*, **7**, 3425-3446.

Luo, Y., K.-M. Xu, H. Morrison, and G. McFarquhar, 2008a: Arctic mixed-phase clouds simulated by a cloud-resolving model: Comparison with ARM observations and sensitivity to microphysics parameterization. *J. Atmos. Sci.*, in press.

Luo, Y., K.-M. Xu, H. Morrison, G. McFarquhar, Z. Wang, and G. Zhang, 2008b: Arctic mixed-phase clouds simulated by a cloud-resolving model: Comparison with ARM observations and sensitivity experiments. *J. Geophys. Res.*, in press.

McFarquhar, G. M. and S. G. Cober, 2004: Single-scattering properties of mixed-phase Arctic clouds at solar wavelengths: Impacts on radiative transfer. *J. Clim.*, **17**, 3799–3813.

McFarquhar, G. and Coauthors, 2007a: The importance of small ice crystals to cirrus properties: Observations from the Tropical Western Pacific International Cloud Experiment (TWP-ICE). *Geophys. Res. Lett.*, **34**, L13803, doi:10.1029/2007GL029865.

McFarquhar, G. and Coauthors, 2007b: Ice properties of single layer boundary clouds during the Mixed-Phase Arctic Cloud Experiment (M-PACE): Part I. Observations. *J. Geophys. Res.*, **112**, D24201, doi:10.1029/2007JD008633.

Meyers, M. P., R. L. Walko, J. Y. Harrington, and W. R. Cotton, 1997: New RAMS cloud microphysics prameterization. Part II: The two-moment scheme. *Atmos. Res.*, **45**,

3-39.

Morrison, H., M. D. Shupe, and J. A. Curry, 2003: Modeling clouds observed at SHEBA using a bulk microphysics parameterization implemented into a single-column model. *J. Geophys. Res.*, **108**, 4255, doi:10.1029/2002JD002229.

Morrison, H., J. A. Curry, and V. I. Khvorostyanov, 2005a: A new double-moment microphysics parameterization for application in cloud and climate models. Part I: Description. *J. Atmos. Sci.*, **62**, 1665-1677.

Morrison, H., J. A. Curry, M. D. Shupe, and P. Zuidema, 2005b: A new double-moment microphysics parameterization for application in cloud and climate models. Part II: Single-column modeling of Arctic clouds. *J. Atmos. Sci.*, **62**, 1678-1693.

Morrison, H. and J. O. Pinto, 2006: Intercomparison of bulk cloud microphysics schemes in mesoscale simulations of springtime Arctic mixed-phase stratiform clouds. *Mon. Wea. Rev.*, **134**, 1880–1900.

Morrison, H. and A. Gettelman, 2008: A new two-moment stratiform cloud microphysics parameterization for the Community Atmosphere Model (CAM3). Part I: Description and numerical tests. *J. Clim.*, in press.

Morrison, H., J. O. Pinto, J. A. Curry, and G. M. McFarquhar, 2008a: Sensitivity of M-PACE mixed-phase stratocumulus to cloud condensation and ice nuclei over regionally-

varying surface conditions. *J. Geophys. Res.*, submitted.

Morrison, H. and Coauthors, 2008b: Intercomparison of model simulations of mixed-phase clouds observed during the ARM Mixed-Phase Arctic Cloud Experiment. Part II: Multi-layer cloud. *Quart. J. Roy. Meteor. Soc.*, submitted.

Neggers, R. A. J., M. Köhler, and A. Beljaars, 2008: A dual mass flux scheme for boundary layer convection. Part I: Transport. *J. Atmos. Sci.*, submitted.

Pinto, J. O., 1998: Autumnal mixed-phase cloudy boundary layers in the Arctic. *J. Atmos. Sci.*, **55**, 2016–2038.

Pinto, J. O., J. A. Curry, and J. M. Intrieri, 2001: Cloud-aerosol interactions during autumn over Beaufort Sea, *J. Geophys. Res.*, **106**, 15077–15098.

Prenni, A. J. and Coauthors, 2007: Can ice-nucleating aerosols affect Arctic seasonal climate? *Bull. Amer. Met. Soc.*, **88**, 541-550.

Randall, D. A. and Coauthors, 2003: Confronting models with data: The GEWEX Cloud Systems Study. *Bull. Amer. Met. Soc.*, **84**, 455–469.

Roeckner, E. and Coauthors, 2003: The atmospheric general circulation model ECHAM5. Part I: Model description. Report 349, Max Planck Institute for Meteorology, Hamburg, Germany, available from http://www.mpimet.mpg.de.

1 Rotstayn, L. D., 1997: A physically based scheme for the treatment of stratiform clouds
2 and precipitation in large-scale models. I: Description and evaluation of the
3 microphysical processes. *Quart. J. Roy. Meteor. Soc.*, **123**, 1227-1282.

4 Rotstayn, L. D., B. F. Ryan, and J. J. Katzfey, 2000: A scheme for calculation of the
5 liquid fraction in mixed-phase stratiform clouds in large-scale models. *Mon. Wea. Rev.*,
6 **128**, 1070–1088.

7 Schmidt, G. A. and Coauthors, 2006: Present day atmospheric simulations using GISS
8 Model E: Comparison to in-situ, satellite and reanalysis data. *J. Clim.*, **19**, 153-192.

9 Shupe, M. D., and J. M. Intrieri, 2004: Cloud radiative forcing of the Arctic surface: The
10 influence of cloud properties, surface albedo, and solar zenith angle. *J. Clim.*, **17**, 616–
11 628.

12 Shupe, M. D., S. Y. Matrosov, and T. Uttal, 2006: Arctic mixed-phase cloud properties
13 derived from surface-based sensors at SHEBA. *J. Atmos. Sci.*, **63**, 697–711.

14 Shupe, M. D., 2007: A ground-based multiple remote-sensor cloud phase classifier.
15 *Geophys. Res. Lett.*, **34**, L22809, doi:10.1029/2007GL031008.

16 Shupe, M. D., P. Kollias, M. Poellot, and E. Eloranta, 2008: On deriving vertical air
17 motions from cloud radar Doppler spectra. *J. Atmos. Ocean. Technol.*, in press.

18 Shutts, G. J. and M. E. B. Gray, 1994: A numerical modelling study of the

geostrophic adjustment process following deep convection. *Quart. J. Roy. Met. Soc.*, **120**, 1145-1178.

Stephens, G. L., 1978: Radiation profiles in extended water clouds. II: Parameterization schemes. *J. Atmos. Sci.,* **35**, 2123-2132.

Stevens, B. and Coauthors, 2005: Evaluation of large-eddy simulations via observations of nocturnal marine stratocumulus. *Mon. Wea. Rev.*, **133**, 1443–1462.

Stull, R. B., 1988: An introduction to boundary layer meteorology. *Kluwer Academic Publishers*, 355 pp.

Sud, Y. C. and D. Lee, 2007: Parameterization of aerosol indirect effect to complement McRAS cloud scheme and its evaluation with the 3-year ARM-SGP analyzed data for single column models. *Atmos. Res.*, accepted.

Sun, Z. and K. Shine, 1994: Studies of the radiative properties of ice and mixed-phase clouds. *Quart. J. Roy. Meteor. Soc.*, **120**, 111–137.

Tripoli, G. J., 1992: A non-hydrostatic mesoscale model designed to simulate scale interaction. *Mon. Wea. Rev.*, **120**, 1342-1359.

Turner, D. D., 2005: Arctic mixed-phase cloud properties from AERI-lidar observations: Algorith and results from SHEBA. *J. Appl. Meteor.,* **44**, 427-444.

Turner, D. D. and Coauthors, 2007: Retrieving liquid water path and precipitable water vapor from Atmospheric Radiation Measurement (ARM) microwave radiometers. *IEEE Trans. Geosci. Remote Sens.*, **45**, 3680-3690, doi:10.1109/TGRS.2007.903703.

Uttal, T. and Coauthors, 2002: Surface Heat Budget of the Arctic Ocean. *Bull. Amer. Met. Soc.*, **83**, 255–275.

Verlinde, H. and Coauthors, 2007: The Mixed-Phase Arctic Cloud Experiment (M-PACE). *Bull. Amer. Met. Soc.*, **88**, 205-221.

von Salzen, K., 2005: Piecewise log-normal approximation of size distributions for aerosol modeling. *Atmos. Chem. Phys.*, **5**, 3959-3998.

Wang, Z. and K. Sassen, 2002: Cirrus cloud microphysical property retrieval using lidar and radar measurements. Part II: Midlatitude cirrus microphysical and radiative properties. *J. Atmos. Sci.*, **59**, 2291-2302.

Wang, Z., 2007: A refined two-channel microwave radiometer liquid water path retrieval for cold regions by using multiple-sensor measurements, *IEEE Geo. Rem. Sens. Lett.*, **4**, 591-595.

Xie, S. and Coauthors, 2006: An assessment of the ECMWF model over the Arctic land using observations from the ARM Mixed-Phase Arctic Cloud Experiment. *J. Geophys. Res.*, **111**, D05107, doi:10.1029/2005JD006509.

Xie, S. and Coauthors, 2008: Simulations of Arctic Mixed-Phase clouds in forecasts with CAM3 and AM2 for M-PACE. *J. Geophys. Res.,* accepted.

Xu, K.-M. and S. K. Krueger, 1991: Evaluation of cloudiness parameterizations using a cumulus ensemble model. A non-hydrostatic mesoscale model designed to simulate scale interaction. *Mon. Wea. Rev.*, **119**, 342-367.

Yuan, J., Q. Fu and N. McFarlane, 2006: Tests and improvements of GCM cloud parameterizations using the CCCMA SCM with the SHEBA data set. *Atmos. Res.*, **82**, 222–238.

Zhao Q. Y., and F. H. Carr, 1997: A prognostic cloud scheme for operational NWP models. *Mon. Wea. Rev.*, **125**, 1931–1953.

Zhu P. and Coauthors, 2005: Intercomparison and interpretation of single-column model simulations of a nocturnal stratocumulus-topped marine boundary layer. *Mon. Wea. Rev.*, **133**, 2741-2758.

Zuidema, P. and Coauthors, 2005: An Arctic springtime mixed-phase cloudy boundary layer observed during SHEBA. *J. Atmos. Sci.*, **62**, 160–176.

Table 1

Characteristics of participating single-column models. For prognostic cloud variables, q_l, q_i, q_r, q_s, and q_g are the mixing ratio of cloud liquid, cloud ice, rain, snow and graupel, respectively. q_c is the mixing ratio of cloud condensate and is equal to the sum of q_l and q_i. N_l, N_i, N_r, N_s and N_g are the number concentrations of cloud liquid, cloud ice, snow and graupel, respectively. In the table, T, PBL, and std are abbreviations for temperature, planetary boundary layer and standard, respectively. For purposes of this table, the height of the planetary boundary layer is defined as 1350 m.

Model	*Investigator and Model reference*	*Cloud microphysics*	*Prognostic cloud variables*	*Do clouds depend on aerosols?*	*# of vertical levels in the PBL at std (high) resolution*
ARCSCM	Hugh Morrison *Morrison et al. (2003)*	double moment *Morrison et al. (2005a)*	q_l, q_i, q_r, q_s N_l, N_i, N_r, N_s	Yes	10 (20)
CCCMA	Jason Cole Knut von Salzen *von Salzen (2005)*	single moment with independent liquid and ice *von Salzen (2005)*	q_l, q_i	Yes (liquid only)	10 (16)
ECHAM	Corinna Hoose *Roeckner et al. (2003)*	double moment *Lohmann et al. (2007)*	q_l, q_i N_l, N_i	Yes	6 (23)
ECMWF	Roel Neggers *ECMWF (2007)*	single moment with T-dependent partitioning (12% liquid at –15°C) *ECMWF (2007)*	q_c	No	14
ECMWF-DUALM	Roel Neggers *Neggers et al. (2008)*	single moment with T-dependent partitioning (12% liquid at –15°C) *ECMWF (2007)*	q_c	No	14
GFDL	Stephen Klein *GFDL GAMDT (2004)*	single moment with independent liquid and ice *Rotstayn et al.(2000)*	q_l, q_i	No	9 (34)
GISS	Audrey Wolf Anthony DelGenio *Hansen et al. (2002)*	single moment with independent liquid and ice *Schmidt et al. (2006)*	q_l, q_i	No	6

Model	*Investigator and Model reference*	*Cloud microphysics*	*Prognostic cloud variables*	*Do clouds depend on aerosols?*	*# of vertical levels in the PBL at std (high) resolution*
GISS-LBL	Igor Sednev Surabi Menon *Hansen et al. (2002)*	bin microphysics *Khain and Sednev (1996)*	33 bins each for liquid droplets, plates, columns, dendrites, snow, graupel, and frozen drops	Yes	8
MCRAS	Yogesh Sud Gregory Walker *Sud and Lee (2007)*	single moment with T-dependent partitioning (75% liquid at –15°C) *Sud and Lee (2007)*	q_c , N_l	Yes (liquid only)	4 (15)
MCRASI	Yogesh Sud Gregory Walker *Sud and Lee (2007)*	double moment *Liu and Penner (2005)*	q_l , q_i N_l , N_i	Yes	4 (15)
NCEP	Fanglin Yang *EMC (2003)*	Single moment with T-dependent partitioning (25% liquid at –15°C) *Zhao and Carr (1997)*	q_c	No	12 (128)
SCAM3	Shaocheng Xie *Collins et al. (2006)*	single moment with T-dependent partitioning (83% liquid at –15°C) *Boville et al. (2006)*	q_c	No	4 (14)
SCAM3-LIU	Xiaohong Liu *Collins et al. (2006)*	double moment *Liu et al. (2007a)*	q_l , q_i N_l , N_i	Yes	4 (14)
SCAM3-MG	Hugh Morrison *Collins et al. (2006)*	double moment *Morrison and Gettelman (2008)*	q_l , q_i N_l , N_i	Yes	4
SCAM3-UW	Sungsu Park *Bretherton and Park (2007)*	single moment with T-dependent partitioning (83% liquid at –15°C) *Boville et al. (2006)*	q_c	No	7 (125)
SCRIPPS	Michael Foster Dana Veron *Iacobellis and Somerville (2006)*	single moment with independent liquid and ice *Rotstayn (1997)*	q_l , q_i	No	7 (17)
UWM	Michael Falk Vincent Larson *Golaz et al. (2002)*	single moment with independent liquid and ice *Larson et al. (2006)*	q_l , q_i	No	51 (146)

Table 2

As in Table 1 but for participating cloud-resolving models. The dimensionality of the model is listed as two-dimensional (2D) or three-dimensional (3D). q_p is the mixing ratio of precipitating condensate and is equal to the sum of q_r, q_s, and q_g.

Model	*Investigator and Model reference*	*Cloud microphysics*	*Prognostic cloud variables*	*Do clouds depend on aerosols ?*	*Dimensionality, Horizontal (std vertical) resolution, Domain size*	*# of vertical levels in the PBL at std (high) resolution*
COAMPS®	Jean-Christophe Golaz Jerome Schmidt *Golaz et al. (2005)*	double moment *Chen et al. (2003)*	q_l, q_i, q_r, q_s, q_g N_l, N_i, N_r	No	3D 50m (20m) 4.8km by 4.8km	67
DHARMA	Ann Fridlind Andy Ackerman *Ackerman et al. (2004)*	bin microphysics *Fridlind et al. (2007)*	20 liquid, 20 ice, and 40 dissolved solute bins	Yes	3D 50m (21m) 3.2km by 3.2km	64
METO	Ben Shipway *Shutts and Gray (1994)*	double moment *Ferrier (1994)*	q_l, q_i, q_r, q_s, q_g N_i, N_s, N_g	No	3D 50m (50m) 6.4km by 6.4km	27 (53)
NMS-BULK	Gijs deBoer Tempei Hashino *Tripoli (1992)*	double moment *Flatau et al. (1989)*	q_l, q_i, q_r, q_s, q_g N_l, N_i, N_r, N_s, N_g	No	2D 200m (100m) 60 km	13
NMS-SHIPS	Gijs deBoer Tempei Hashino *Tripoli (1992)*	bin microphysics *Hashino and Tripoli (2007)*	21 liquid, 20 ice and 1 aerosol bins	Yes (ice only)	2D 200m (100m) 60km	13
RAMS-CSU	Alex Avramov Jerry Harrington *Cotton et al. (2003)*	double moment *Meyers et al. (1997)*	q_l, q_i, q_r, q_s, q_g N_l, N_i, N_s, N_g	Yes (ice only)	2D 1000m (70m) 150km	17 (29)
SAM	Mingxuan Chen Marat Khairoutdinov *Khairoutdinov and Randall (2003)*	single moment with T-dependent partitioning (25% liquid at –15°C) *Khairoutdinov and Randall (2003)*	q_c, q_p	No	3D 100m (50m) 12.7km by 12.7km	27 (53)
UCLA-LARC	Yali Luo Kuan-Man Xu *Luo et al. (2008a)*	double moment *Morrison et al. (2005a)*	q_l, q_i, q_r, q_s N_l, N_i, N_r, N_s	Yes	2D 2km (180m) 256km	7 (23)
UCLA-LARC-LIN	Yali Luo Kuan-Man Xu *Xu and Krueger (1991)*	single moment with independent liquid and ice *Lin et al. (1983)*	q_l, q_i, q_r, q_s, q_g	No	2D 2km (180m) 256 km	7 (23)

Table 3

Median condensate water paths and inter-quartile ranges in parentheses from observations for the study period.

	Liquid water path ($g\ m^{-2}$)	Ice water path ($g\ m^{-2}$)
Aircraft		
Flight 1009	130.1 (94.2-143.2)	8.0 (4.7-16.4)
Flight 1010a	109.3 (101.2-116.9)	3.5 (2.5-11.7)
Combined flights	115.3 (98.3-135.7)	7.6 (3.4-14.7)
Ground-based		
SHUPE-TURNER @ Barrow	224.2 (172.3-280.8)	30.7 (19.2-42.8)
WANG @ Barrow	195.6 (141.2-251.3)	28.1 (22.3-38.0)
TURNER @ Oliktok Point	87.6 (69.1-103.5)	
WANG @ Oliktok Point	127.9 (102.0-151.6)	

Table 4

Median condensate water paths from models for simulation hours four through twelve. Results are reported for the standard experiment as well as sensitivity experiments in which ice microphysics are disabled and higher vertical resolution employed. Where available, the rain, snow, graupel water paths are included the reported total liquid and ice water paths. Asterisks (*) indicate SCMs for which the rain and snow water paths were unavailable. Median SCM ice water paths are computed using only models which report snow water paths.

	Liquid water path (g m^{-2})			Ice water path (g m^{-2})	
	Standard	No ice	High Resolution	Standard	High Resolution
Median model	56.7	208.0	63.1	25.9	26.0
Median SCM	56.0	256.2	64.4	29.1	35.9
Median CRM	57.3	183.6	63.1	17.1	22.8
Median model with single moment with T-dependent partitioning microphysics	21.2	258.6	21.7	33.8	35.9
Median model with single moment with independent liquid and ice microphysics	72.8	263.1	63.1	31.8	28.8
Median model with double moment microphysics	100.0	183.6	195.7	19.9	10.3

	Liquid water path (g m^{-2})			Ice water path (g m^{-2})	
Median model with bin microphysics	69.1			17.0	
SCMs					
ARCSCM	291.8	358.6	306.0	11.8	9.9
CCCMA	264.9	269.9	336.5	11.5	1.2
ECHAM*	165.5	164.4	239.8	1.0	2.5
ECMWF	5.8			55.9	
ECMWF-DUALM	21.2			171.2	
GFDL	51.0	278.8	35.0	29.2	27.6
GISS*	47.8			20.8	
GISS-LBL	29.8	187.8		26.0	
MCRAS*	13.7	309.1	8.7	2.6	1.2
MCRASI*	20.1	577.8	8.9	2.7	11.3
NCEP*	16.1	60.6	21.7	39.6	56.6
SCAM3	172.9		233.6	28.8	35.9
SCAM3-LIU	144.5		40.0	31.1	131.5
SCAM3-MG	56.0			24.0	
SCAM3-UW	172.9	208.0	126.5	29.1	62.2
SCRIPPS*	112.0	140.4	49.0	13.5	12.3
UWM	88.2	256.2	79.8	37.0	36.0
CRMs					
COAMPS®	24.1	267.3		25.7	
DHARMA	135.7	217.8		17.0	
METO	29.7	77.6	36.7	22.7	24.3
NMS-BULK	1.6	82.0		17.1	
NMS-SHIPS	69.1	65.2		0.03	
RAMS-CSU	172.6	172.8	222.4	0.007	0.014
SAM	23.3	328.5	20.2	33.8	22.8
UCLA-LARC	167.5	194.4	195.7	8.4	10.3
UCLA-LARC-LIN	57.3		63.1	34.4	30.0

Figure captions

Figure 1. Moderate resolution imaging spectroradiometer composite visible image of the North slope of Alaska and Beaufort Sea for October 9, 2004. The boundary layer clouds occurred when cold air above the sea ice to the northeast of Alaska flowed over the ice-free Beaufort Sea inducing the significant surface heat fluxes responsible for cloud formation. The sea ice is visible in the upper right corner of the image. The clouds were observed in the northeasterly flow between the ARM stations of Barrow and Oliktok Point on the coast of snow-covered Alaska. As is common in "cold-air outbreak" stratocumulus, boundary layer "rolls" or "cloud streets" developed with a horizontal scale that increases in the downstream direction.

Figure 2. Initial conditions for model simulations of the potential temperature (right panel, thick line) and mixing ratios of water vapor (left panel, thick line) and cloud liquid (left panel, dashed line). Also shown are the values of the potential temperature (right panel, thin line) and water vapor mixing ratio (left panel, thin line) from the 17Z 9 October 2004 sounding at Barrow. The triangle in the right panel indicates the value of the ocean surface potential temperature in the coastal region.

Figure 3. Vertical pressure velocity (Omega) and the horizontal advective tendencies of temperature and water vapor mixing ratio for the period 17Z 9 October to 5Z 10 October 2004. Each panel displays the values from the ECMWF analysis (solid line) and the

values used in the model simulations (dots).

Figure 4. Time-averaged cloud fraction from observations and models as a function of height. The observations panel depicts the fraction of time at each height that cloud was observed from remote sensors at Barrow (SHUPE-TURNER) and the two aircraft flights during the period 17Z 9 October to 5Z 10 October 2004. Model panels depict statistical properties of the mean cloud fraction for hours four through twelve of model simulations. The properties depicted include the median of models (solid black line), the inner 50% of models (dark shading), and the outer 50% of models (light shading).

Figure 5. Time averaged hydrometeor fraction from models and the remote sensors at Barrow (SHUPE-TURNER, dashed line).

Figure 6. Time-averaged fraction of observations with a given phase as a function of normalized height. Phase categories include liquid-phase only, ice-phase only, and mixed-phase. Normalized height is defined such that 0 is cloud base, 1 is cloud top, and –1 is the surface. The remote sensor retrievals are from SHUPE-TURNER.

Figure 7. Scatterplot of the median liquid water path and ice water path from observations (letters) and model simulations (symbols). The aircraft observations are depicted by the letter "A", whereas the remote sensing retrievals of SHUPE-TURNER and WANG are depicted by the letters "S" and "W", respectively. The lightly dashed rectangle indicates the likely range of the regionally averaged liquid and ice water path. The filling or lack thereof in a symbol indicates the model type and the symbol

shape indicates the class of model cloud microphysics. See the legend in the plot for the key. As observations do not distinguish between precipitating and non-precipitating condensate, the reported water paths include the contributions from the precipitating species. SCMs for which the precipitation species were unavailable are indicated with a "*" in the center of the symbol. One model falls outside the plot regions and is depicted with a "↑" attached to its symbol which points to the numerical value of the ordinate. A 1:1 line is plotted for reference.

Figure 8. Liquid water content from models and aircraft data as a function of normalized height. Each panel depicts the statistical properties of the profiles including the median value, and the inner and outer 50% of the data as in Figure 4. For the aircraft data, the statistical properties are computed from the high-frequency data. For the models, the statistical properties are computed from the set of model median profile values.

Figure 9. As in Figure 8 but for ice water content. The remote sensing retrievals are from WANG. Note that there are no aircraft data at normalized heights less than –0.6. The SCM plot is constructed by only using the models which report snow water paths.

Figure 10. Cloud microphysical properties from aircraft observations and models. For the aircraft observations, the plot displays the statistical properties of the mass-weighted values for each profile. The statistical properties include the median value (black line), inner and outer 50% of profile values (heavy and light shading, respectively). For the models, the depicted values are mass-weighted values and averaged over time and height.

Symbols are plotted with the same convention as in Figure 7.

Figure 11. The vertical profiles of total water mixing ratio ratio q_t and ice-liquid water potential temperature θ_{li} from the models. Each panel depicts the statistical properties (median, inner and outer 50%) of the model median profiles as well as the values from the initial condition.

Figure 12. Scatterplot of solar transmission and total condensate water path. Solar transmission is computed as the average downward component to the broadband solar radiation at the surface divided by the average insolation at the top-of-the-atmosphere. Model results are indicated with symbols with the same convention as in Figure 7. The observations from the radiation measurements and remote sensing retrievals at Barrow are indicated by OBS. The results of STREAMER radiation calculations performed with an ice-free ocean or snow-covered land surface are indicated by S-O and S-L, respectively.

Figure 13. As in Figure 12 but for the downward longwave radiative flux at the surface.

Figure 14. Scatterplot of the model simulated liquid water path from a sensitivity study in which ice microphysics were disabled and the total (liquid + ice) condensate water path from the control simulation. A 1:1 line is shown.

Figure 15. Scatterplot of the ratio of the total condensate water path in the no-ice sensitivity study to that of the control simulation and the fraction of the total condensate water path in the control simulation that is in the ice-phase. Note that the y-axis is

logarithmic and that two models fall outside the plot domain.

Figure 16. Scatterplot of the model simulated total (liquid + ice) condensate water path from a sensitivity study in which models used increased vertical resolution and the control simulations.

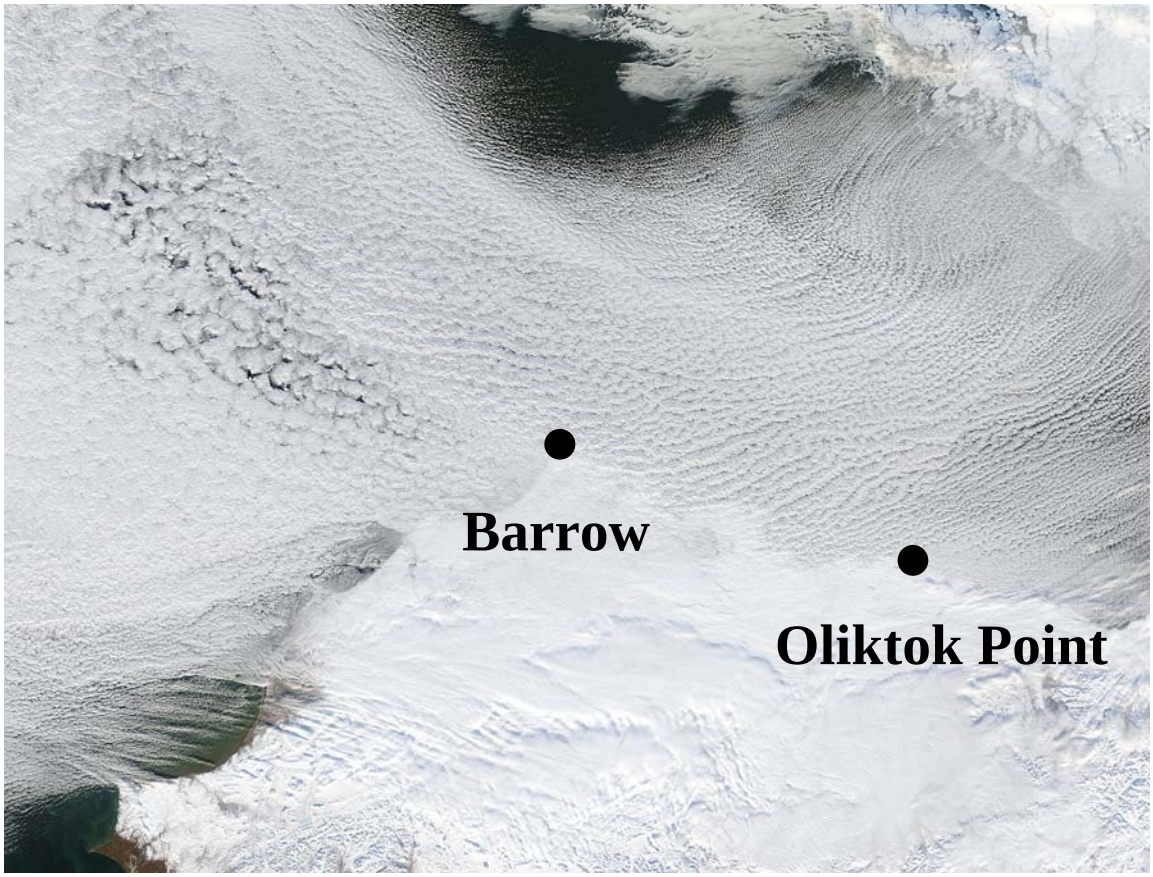

Figure 1. Moderate resolution imaging spectroradiometer composite visible image of the North slope of Alaska and Beaufort Sea for October 9, 2004. The boundary layer clouds occurred when cold air above the sea ice to the northeast of Alaska flowed over the ice-free Beaufort Sea inducing the significant surface heat fluxes responsible for cloud formation. The sea ice is visible in the upper right corner of the image. The clouds were observed in the northeasterly flow between the ARM stations of Barrow and Oliktok Point on the coast of snow-covered Alaska. As is common in "cold-air outbreak" stratocumulus, boundary layer "rolls" or "cloud streets" developed with a horizontal scale that increases in the downstream direction.

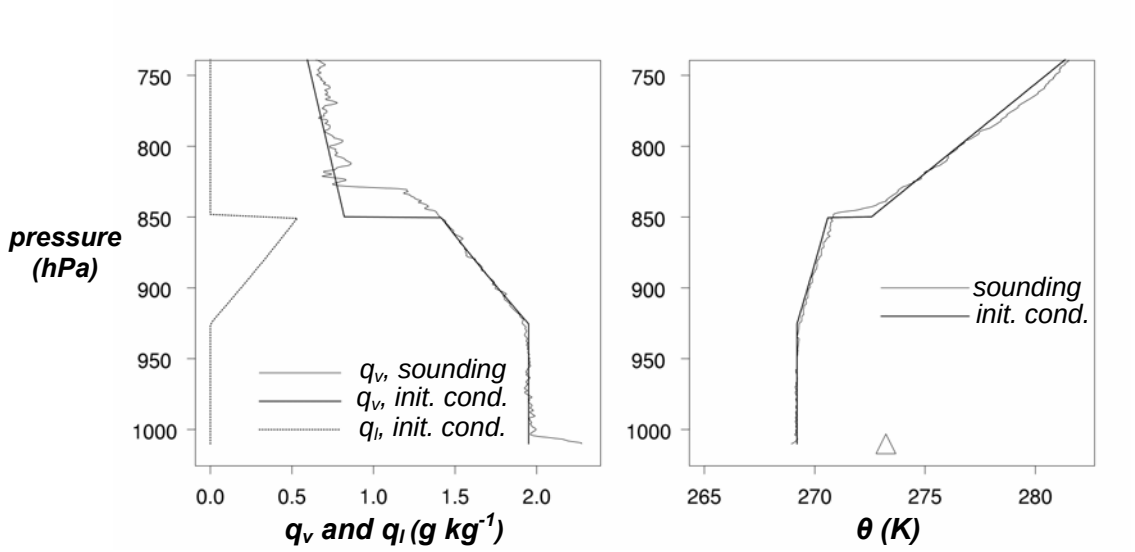

Figure 2. Initial conditions for model simulations of the potential temperature (right panel, thick line) and mixing ratios of water vapor (left panel, thick line) and cloud liquid (left panel, dashed line). Also shown are the values of the potential temperature (right panel, thin line) and water vapor mixing ratio (left panel, thin line) from the 17Z 9 October 2004 sounding at Barrow. The triangle in the right panel indicates the value of the ocean surface potential temperature in the coastal region.

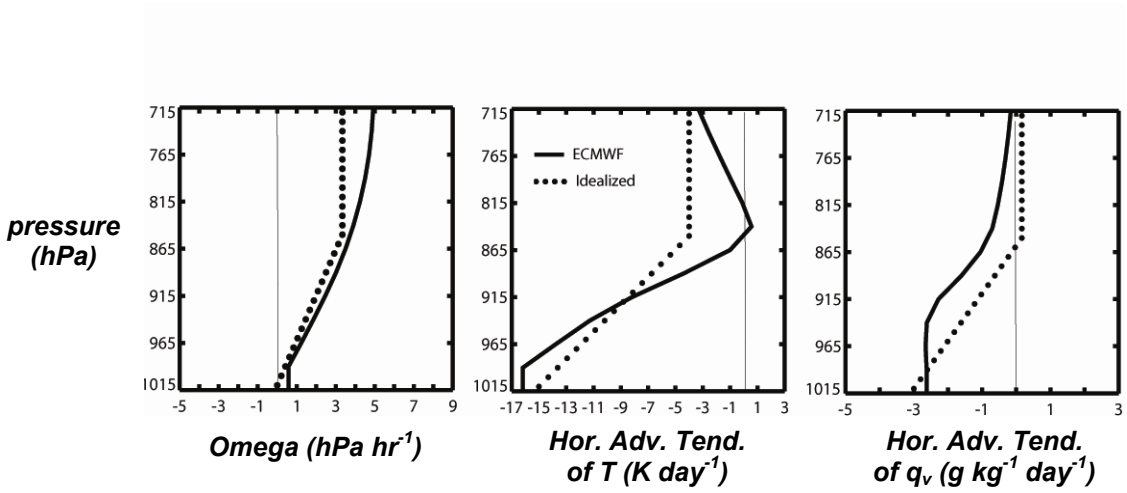

Figure 3. Vertical pressure velocity (Omega) and the horizontal advective tendencies of temperature and water vapor mixing ratio for the period 17Z 9 October to 5Z 10 October 2004. Each panel displays the values from the ECMWF analysis (solid line) and the values used in the model simulations (dots).

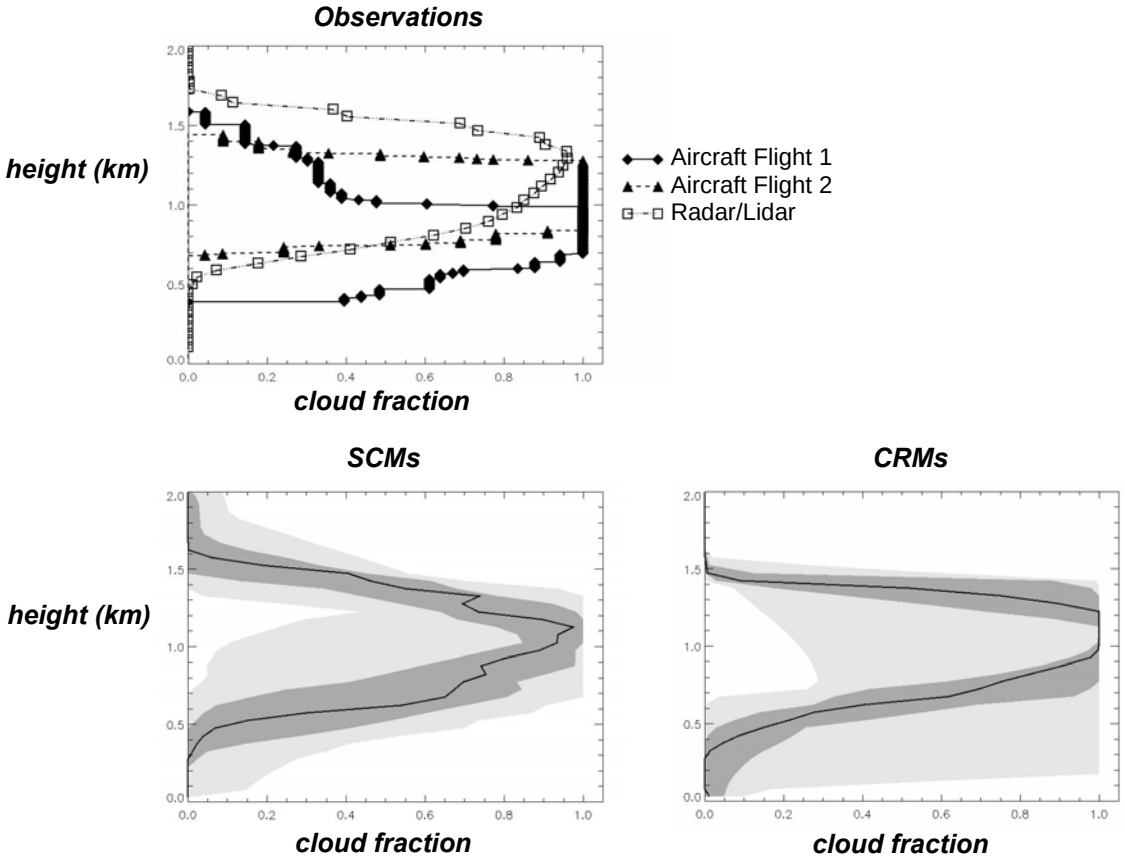

Figure 4. Time-averaged cloud fraction from observations and models as a function of height. The observations panel depicts the fraction of time at each height that cloud was observed from remote sensors at Barrow (SHUPE-TURNER) and the two aircraft flights during the period 17Z 9 October to 5Z 10 October 2004. Model panels depict statistical properties of the mean cloud fraction for hours four through twelve of model simulations. The properties depicted include the median of models (solid black line), the inner 50% of models (dark shading), and the outer 50% of models (light shading).

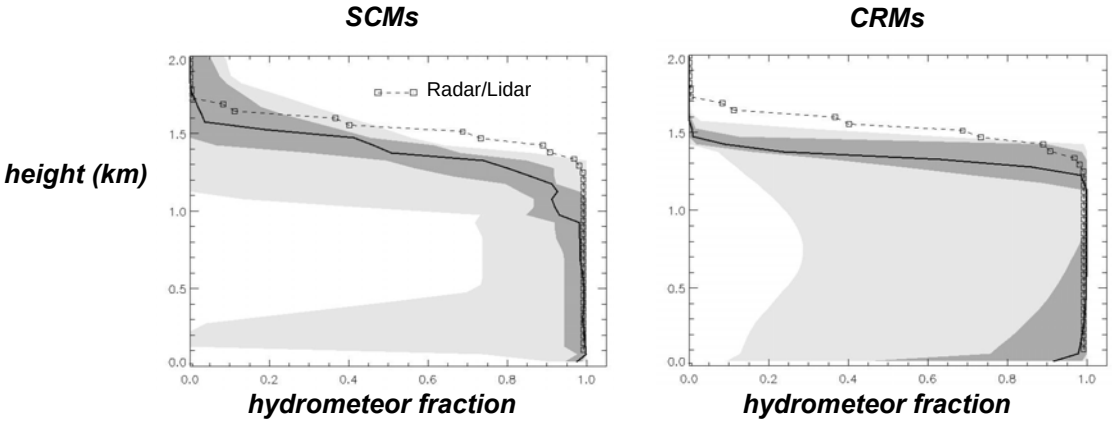

Figure 5. Time averaged hydrometeor fraction from models and the remote sensors at Barrow (SHUPE-TURNER, dashed line).

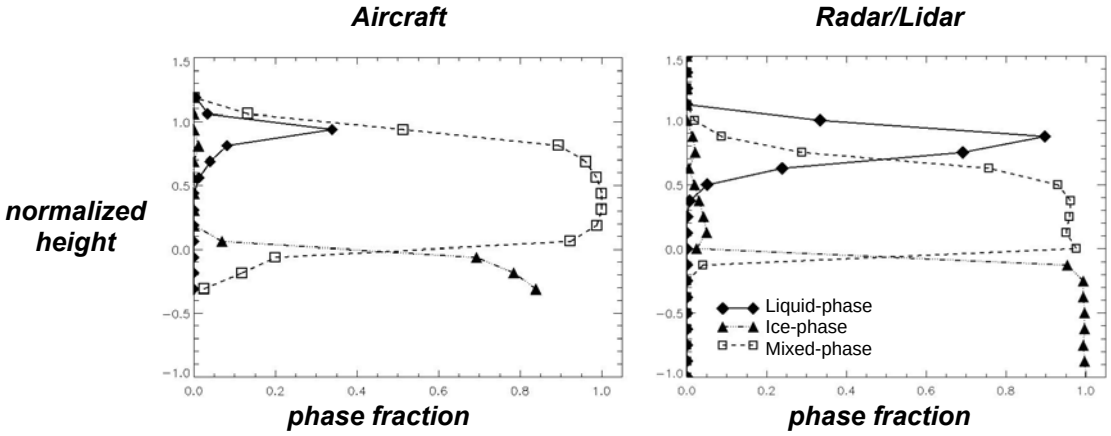

Figure 6. Time-averaged fraction of observations with a given phase as a function of normalized height. Phase categories include liquid-phase only, ice-phase only, and mixed-phase. Normalized height is defined such that 0 is cloud base, 1 is cloud top, and –1 is the surface. The remote sensor retrievals are from SHUPE-TURNER.

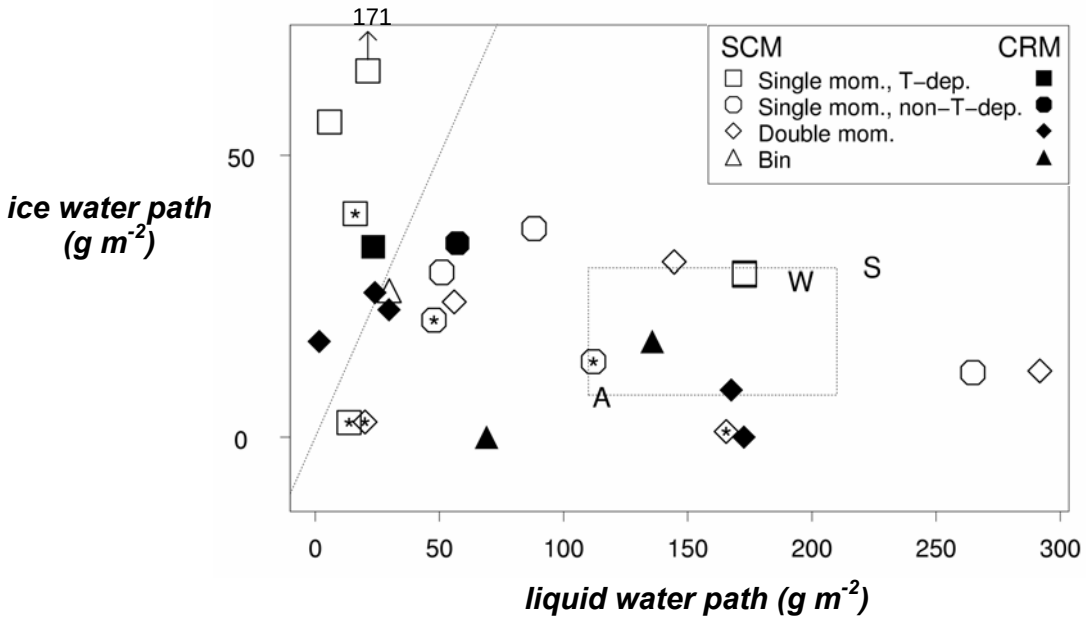

Figure 7. Scatterplot of the median liquid water path and ice water path from observations (letters) and model simulations (symbols). The aircraft observations are depicted by the letter "A", whereas the remote sensing retrievals of SHUPE-TURNER and WANG are depicted by the letters "S" and "W", respectively. The lightly dashed rectangle indicates the likely range of the regionally averaged liquid and ice water path. The filling or lack thereof in a symbol indicates the model type and the symbol shape indicates the class of model cloud microphysics. See the legend in the plot for the key. As observations do not distinguish between precipitating and non-precipitating condensate, the reported water paths include the contributions from the precipitating species. SCMs for which the precipitation species were unavailable are indicated with a "*" in the center of the symbol. One model falls outside the plot regions and is depicted with a "↑" attached to its symbol which points to the numerical value of the ordinate. A 1:1 line is plotted for reference.

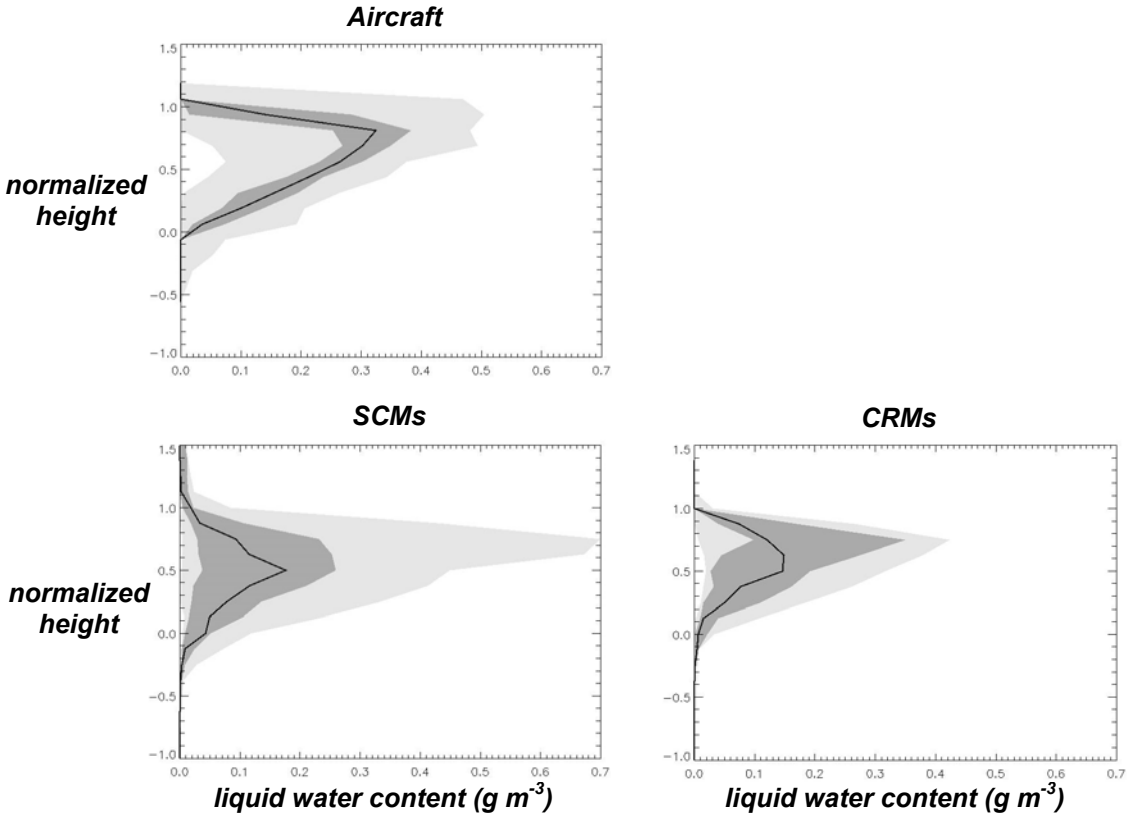

Figure 8. Liquid water content from models and aircraft data as a function of normalized height. Each panel depicts the statistical properties of the profiles including the median value, and the inner and outer 50% of the data as in Figure 4. For the aircraft data, the statistical properties are computed from the high-frequency data. For the models, the statistical properties are computed from the set of model median profile values.

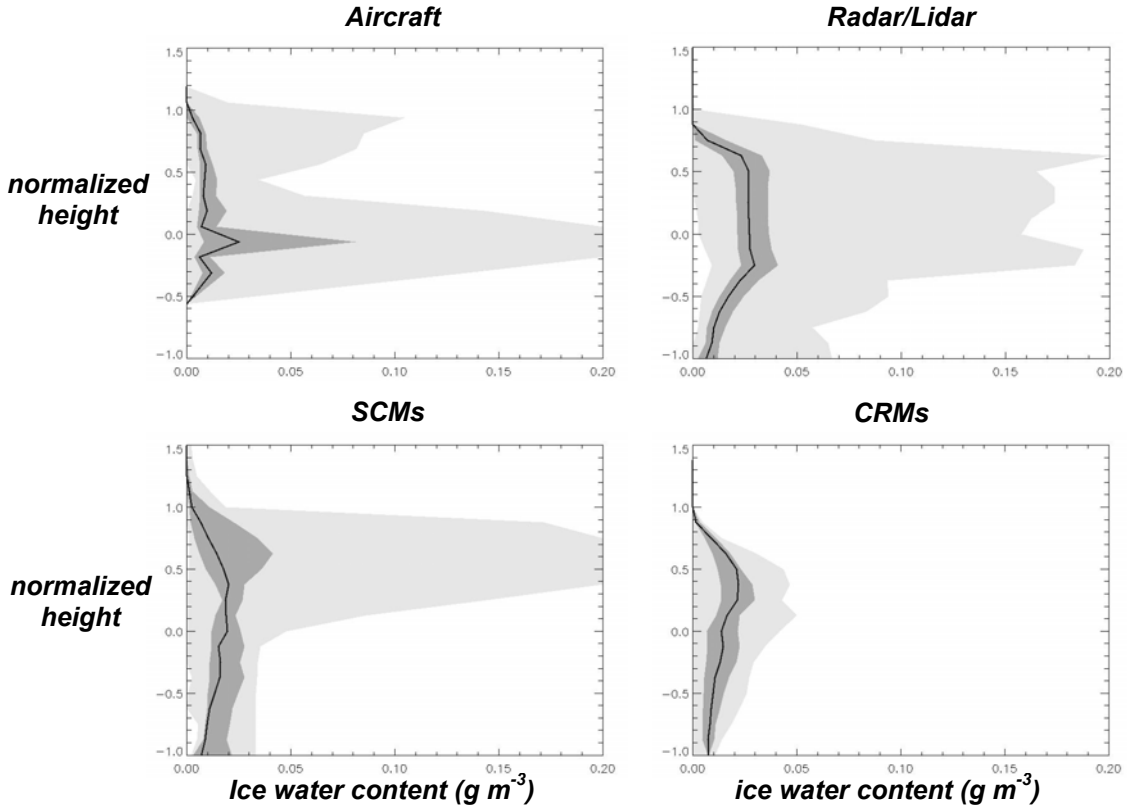

Figure 9. As in Figure 8 but for ice water content. The remote sensing retrievals are from WANG. Note that there are no aircraft data at normalized heights less than –0.6. The SCM plot is constructed by only using the models which report snow water paths.

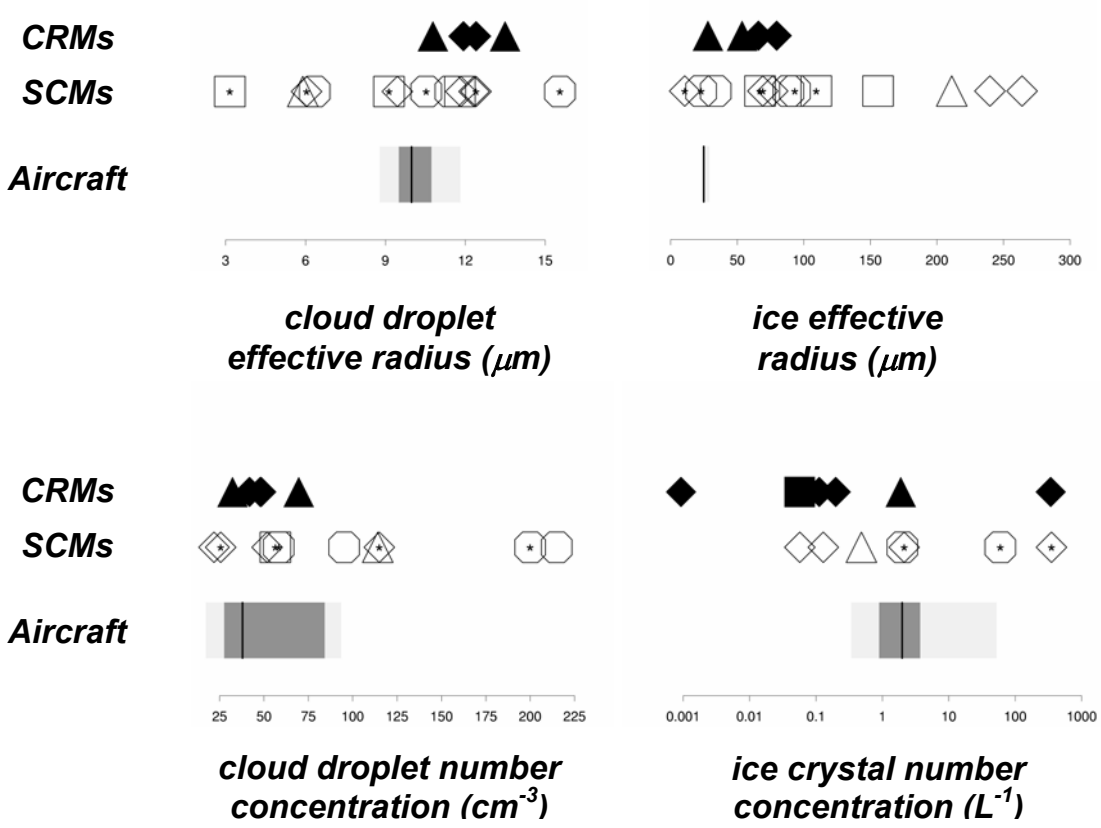

Figure 10. Cloud microphysical properties from aircraft observations and models. For the aircraft observations, the plot displays the statistical properties of the mass-weighted values for each profile. The statistical properties include the median value (black line), inner and outer 50% of profile values (heavy and light shading, respectively). For the models, the depicted values are mass-weighted and averaged over time and height. Symbols are plotted with the same convention as in Figure 7.

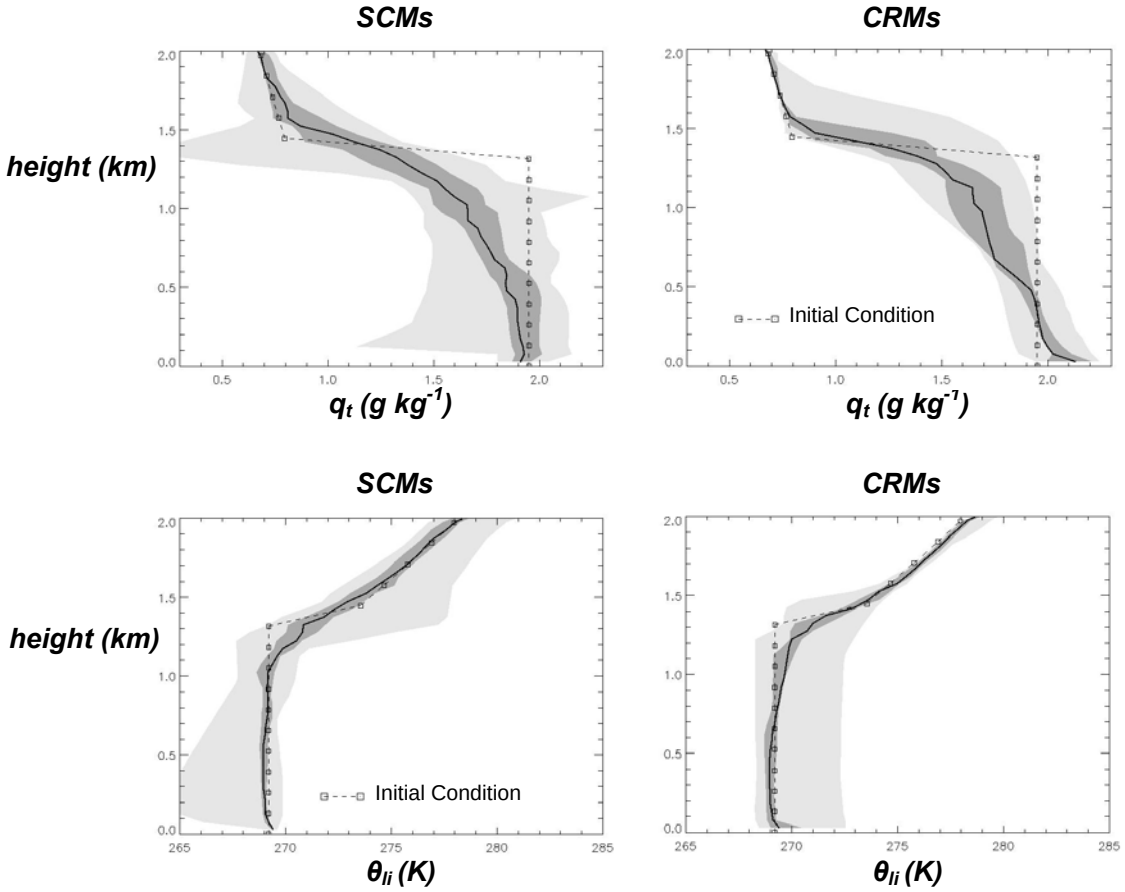

Figure 11. The vertical profiles of total water mixing ratio q_t and ice-liquid water potential temperature θ_{li} from the models. Each panel depicts the statistical properties (median, inner and outer 50%) of the model median profiles as well as the values from the initial condition.

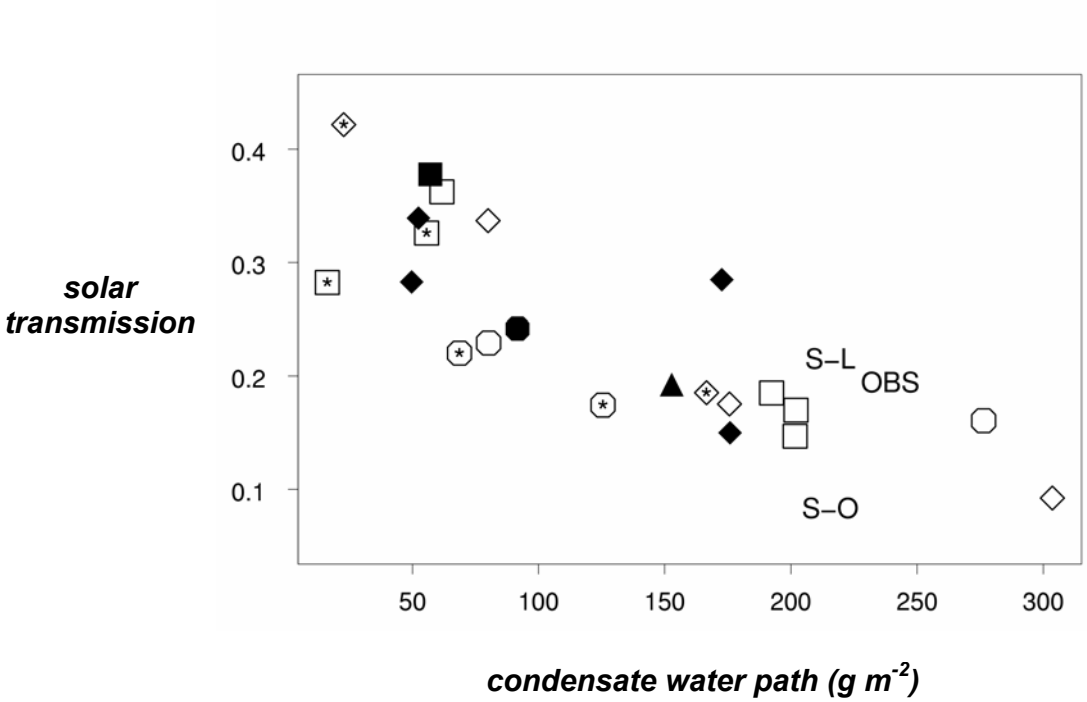

Figure 12. Scatterplot of solar transmission and total condensate water path. Solar transmission is computed as the average downward component to the broadband solar radiation at the surface divided by the average insolation at the top-of-the-atmosphere. Model results are indicated with symbols with the same convention as in Figure 7. The observations from the radiation measurements and remote sensing retrievals at Barrow are indicated by OBS. The results of STREAMER radiation calculations performed with an ice-free ocean or snow-covered land surface are indicated by S-O and S-L, respectively.

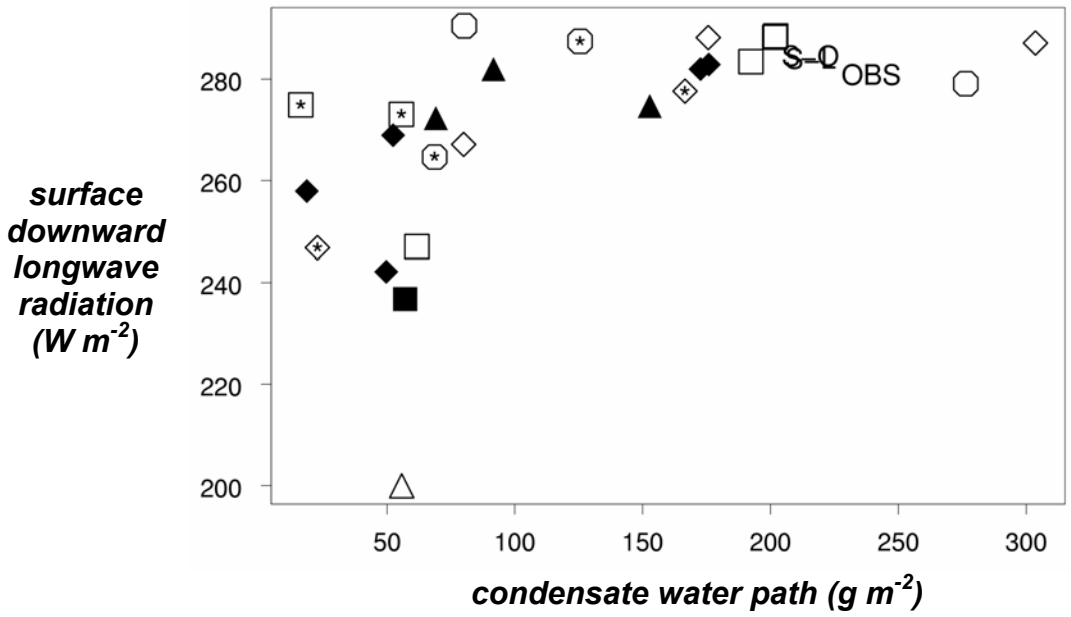

Figure 13. As in Figure 12 but for the downward longwave radiative flux at the surface.

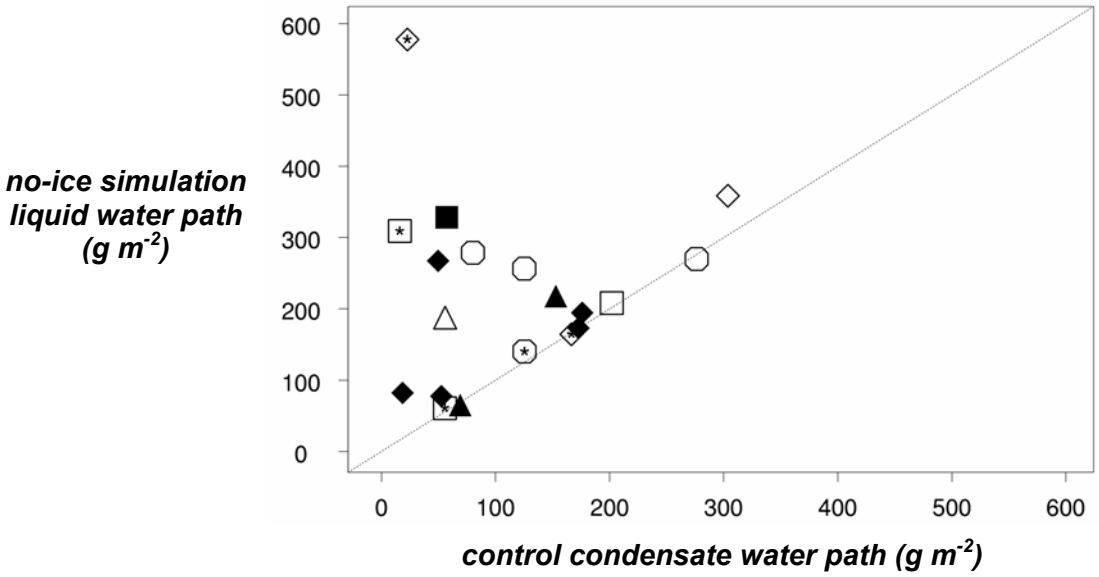

Figure 14. Scatterplot of the model simulated liquid water path from a sensitivity study in which ice microphysics were disabled and the total (liquid + ice) condensate water path from the control simulation. A 1:1 line is shown.

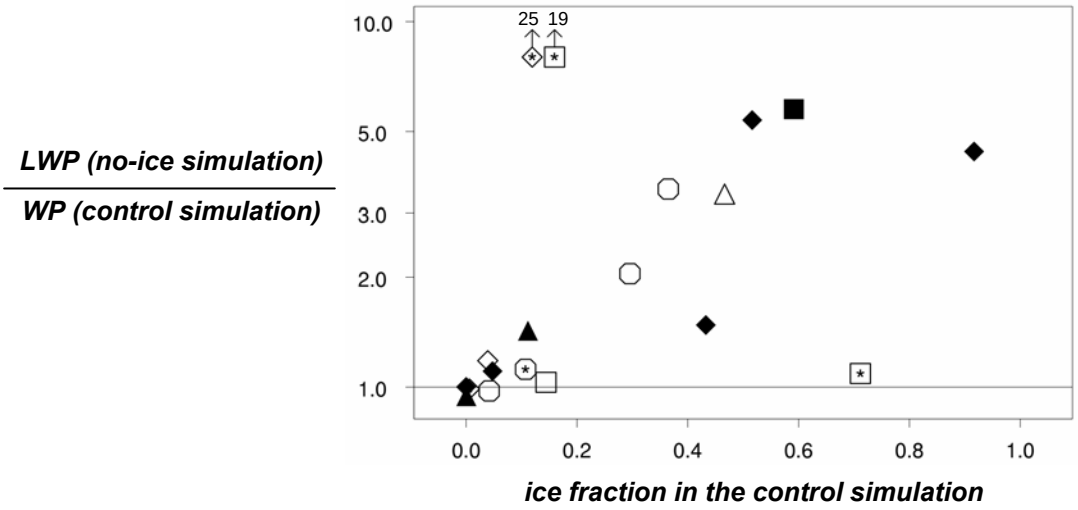

Figure 15. Scatterplot of the ratio of the total condensate water path in the no-ice sensitivity study to that of the control simulation and the fraction of the total condensate water path in the control simulation that is in the ice-phase. Note that the y-axis is logarithmic and that two models fall outside the plot domain.

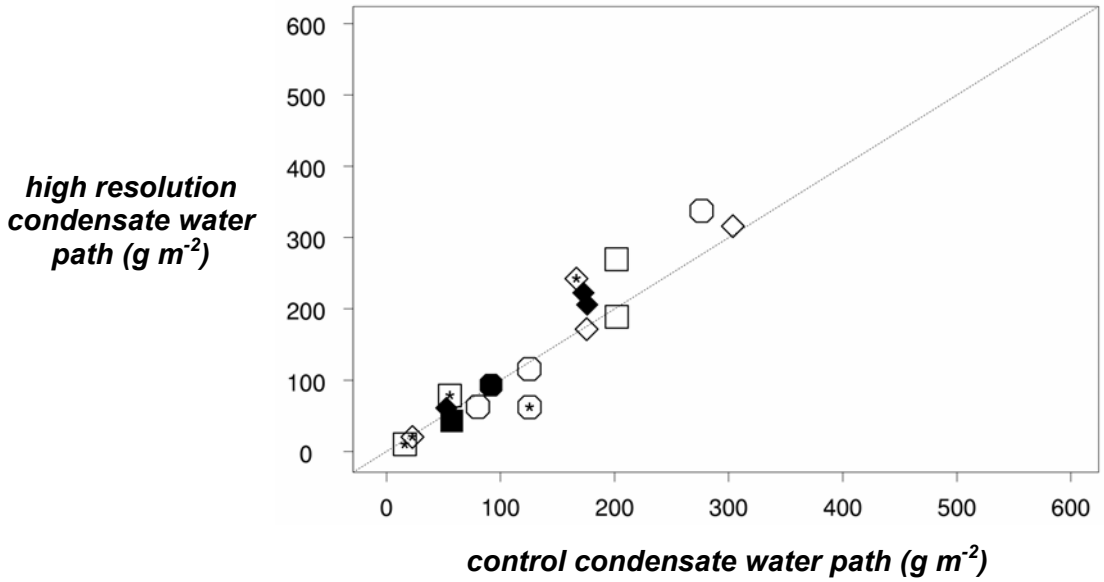

Figure 16. Scatterplot of the model simulated total (liquid + ice) condensate water path from a sensitivity study in which models used increased vertical resolution and the control simulation.